# Beating the Thermodynamic Limit: Photo-Activation of n-Doping in Organic Semiconductors

Xin Lin,[1] Berthold Wegner,[2,3] Kyung M. Lee,[1] Michael A. Fusella,[1] Fengyu Zhang,[1] Karttikay Moudgil,[4] Barry P. Rand,[1] Stephen Barlow,[4] Seth R. Marder,[4] Norbert Koch[2,3] and Antoine Kahn[1]*

**Affiliations:**

[1]Department of Electrical Engineering, Princeton University, Princeton, New Jersey 08544, USA.

[2]Helmholtz-Zentrum Berlin für Materialien und Energie GmbH, Albert-Einstein-Str. 16, D-12489 Berlin, Germany.

[3]Institut für Physik & IRIS Adlershof Humboldt-Universität zu Berlin, Brook-Taylor-Str. 6, D-12489 Berlin, Germany.

[4]Center for Organic Photonics and Electronics and School of Chemistry and Biochemistry, Georgia Institute of Technology, Atlanta, Georgia 30332, USA.

*Correspondence to: kahn@princeton.edu

**Chemical doping of organic semiconductors using molecular dopants plays a key role in the fabrication of efficient organic electronic devices. While a variety of stable molecular p-dopants have been developed and successfully deployed in devices in the past decade, air stable molecular n-dopants suitable for materials with low electron affinity are still elusive. Here we demonstrate that photo-activation of a cleavable air-stable dimeric dopant can result in kinetically stable and efficient n-doping of host semiconductors, whose reduction potentials are beyond the thermodynamic reach of the dimer's effective reducing strength. The performance of these photo-activated dopants exceeds by a considerable margin what is currently available in the field of organic electronics. Electron transport layers doped in this manner are used to fabricate high-efficiency organic light-emitting diodes. Our strategy thus enables a new paradigm for using air-stable molecular dopants to improve conductivity in, and provide ohmic contacts to, very low electron affinity organic semiconductors.**

n-Doping of organic semiconductors involves donation of an electron by a reducing agent to the electron transport level of the semiconductor material. Molecular dopants are preferred in organic electronics because of compatibility of processing with the host, i.e. similar evaporation temperatures or controllable solubility, and powerful molecular n-dopants have therefore been actively researched in the past decade [1–12]. However, air stable molecular n-dopants suitable for materials with low electron affinity (EA) are still elusive, for several reasons. If operating as simple one-electron reductants, these molecules must have an ionization energy (IE) that is close to or lower than the EA of the host material, increasing their susceptibility to oxidation in ambient conditions. n-Doping is particularly challenging for organic semiconductors used as electron-transport materials (ETMs) in OLEDs, which generally have an EA smaller than 3 eV, requiring dopants with comparably low IE [1,13].

A general approach to address this issue involves air-stable precursors (i.e., species with relatively high IE) that liberate strongly reducing species during their insertion into the organic host, or that do not react through simple one-electron transfer, but in a fashion whereby bond cleavage and/or formation accompanies electron transfer. The first approach, which has been used to dope materials with EA ≥ 4.0 eV [14], is exemplified by certain cationic dyes [9,14–18], from which the corresponding neutral radicals (and/or other highly reducing species) sublime when heated in ultra-high vacuum. The second approach involves several classes of materials including (i) molecules that can be regarded, at least formally, as hydride-reduction products of stable organic cations; (ii) tetraalkylammonium salts of simple inorganic ions such as halides; and (iii) dimers formed by certain 19-electron organometallic sandwich compounds or organic radicals. Molecules included in class (i) necessarily react with both transfer of a hydrogen atom and an electron to the host, in some cases only following thermal or photochemical activation [16,18–21]. This class of compounds can be processed from either vacuum or solution and are particularly effective dopants for fullerene derivatives (EA ~ 3.8 to 4.0 eV) [18,19,22,23], but have also been reported to dope poly{[*N,N′*-bis(2-octyldodecyl)-napthalene-1,4,5,8-bis(dicarboximide)-2,6-diyl]-alt-5,5′-(2,2′-bithiophene)} (P(NDIOD-T2), EA ~ 3.9 eV) [20] and 6,13-bis(triisopropylsilylethynyl)pentacene (TIPS-pentacene, EA ~ 3.0 eV) [9], although in the latter case it is likely that the observed change from p- to n-channel behavior can be attributed to trap-filling rather than contribution of "free" carriers [23,24]. Class (ii) dopants have also been found to be effective solution-processable dopants for some fullerenes; the reaction appears to proceed through nucleophilic attack of the anion on a fullerene and so, as with class (i) dopants, side products besides an ETM radical anion and a stable cation are to be expected [25].

Guo et al. [26] recently introduced class (iii) of air-stable dopants, i.e. dimers of highly reducing organometallic species, whereby the air-stable dimer reacts to yield two monomer cations and two electrons. Depending on the dimer and the ETM in question, this process can occur either via a reversible endergonic cleavage of the dimer followed by a rapid exergonic electron transfer, or an endergonic electron transfer followed by a rapid cleavage of the dimer cation and a second electron-transfer reaction [27]. Using these dimers, small-molecule and polymer semiconductors such as $C_{60}$, P(NDIOD-T2), pentacene, and TIPS-pentacene, with EAs ranging down to 2.8 eV, were successfully n-doped [26,28–30]. This EA limit corresponds to the overall thermodynamic reducing ability (i.e. the effective reducing strength) of the dimers, which can be estimated using a combination of cyclic voltammetry (CV) measurements on the corresponding monomer cation salts (in solution) and density functional theory estimates of the free energy of bond dissociation as ca. –2.0 V vs. $FeCp_2^+/FeCp_2$ for a range of these dimers [31]. To date, however, thermal or photochemical stimuli, such as the photo-activation used to dope

$C_{60}$ with leuco crystal violet [16], have not been used to activate solid-state doping by these dimers, although the solution reaction of pentamethyliridocene dimer and TIPS-pentacene is dramatically accelerated by exposure to visible light [31].

We introduce here a fundamental advance in doping employing one of these dimers, based on photo-activation to n-dope materials with EAs significantly lower than 2.8 eV. Under deep red to ultra-violet (UV) irradiation, photo-assisted electron transfer, accompanied by the cleavage of dimers, occurs, generating negatively charged host molecules and positively charged monomers, and thus realizing n-type doping. Although the n-doping is sustained once the irradiation has been turned off, as evidenced by the persistence of the host semiconductor work function (WF) and conductivity for thousands of hours, it is important to point out that the presumed doping products are *thermodynamically* unstable with respect to conversion back to the neutral dimer and neutral host and, therefore, that the observed stability must be due to kinetic factors. The photo-activation of n-doping in very low EA materials with air-stable organometallic dimers is an exceedingly important step forward for organic electronic devices, allowing circumvention of highly reactive and *diffusive* electropositive elements such as alkali metals, which have been routinely used to n-dope low-EA electron-transport materials used in OLEDs [32].

Figure 1A shows the chemical structures of the host, phenyldi(pyren-2-yl)phosphine oxide ($POPy_2$), a typical molecular ETM used in OLEDs [33–35] with an EA of about 2.2 eV (for electronic structure, see Fig. S1), and the dopant, the (pentamethylcyclopentadienyl)(1,3,5-trimethylbenzene)ruthenium dimer ($[RuCp^*Mes]_2$), which has been previously used to n-dope pentacene, TIPS-pentacene, and $C_{60}$ [26,29]. The oxidation potentials of $[RuCp^*Mes]_2$ and its monomer determined by CV-measurements, as well as its effective reducing strength, are given in Fig. 1B and compared to the reduction potential of the $POPy_2$. Since the reduction potential of $POPy_2$ is 0.2 V more anodic than the $[RuCp^*Mes]^+/0.5[RuCp^*Mes]_2$ potential, which measures the dimer's effective reducing strength, the dimer is *unable* to dope $POPy_2$ in a thermodynamically stable fashion (as indicated by equation (b) in Fig. 1D). Fig. 1C shows the optical absorption spectra of a highly doped thin film of $POPy_2$ before and after UV irradiation (375 nm). The large dopant concentration of 33.3% (molar ratio of $POPy_2$:$[RuCp^*Mes]_2$ = 2:1) was chosen with the expectation of obtaining a strong anion feature, easily observable by optical absorption spectroscopy, in the event of any doping. Prior to UV irradiation, the mixed film only shows the absorption of pristine $POPy_2$ with its main feature at 3.4 eV (Fig. S2). Upon irradiation, however, a new feature emerges at 2.4 eV, which increases with irradiation time, while the main feature corresponding to neutral $POPy_2$ is reduced. By comparison with the results from Oyamada et al. [33], the 2.4 eV feature is attributed to the absorption of the $POPy_2$ anion, indicating electron transfer from the dopant to the host. These results therefore show that photo-activation is not only possible, but also needed, to enable the n-doping of $POPy_2$ with $[RuCp^*Mes]_2$.

To investigate the influence of UV irradiation on the doping process, the WF and conductivity of the $POPy_2$ films were measured as a function of $[RuCp^*Mes]_2$ concentration before and after UV activation (Fig. S3), the results of which are summarized in Fig. 2A and Table 1A (the dopant concentration is quantified here using the Ru/O ratio as determined via X-ray photoemission spectroscopy, XPS; see Supplementary Text). The decrease in WF indicates an upward shift of the Fermi level ($E_F$) in the $POPy_2$ gap. Before photo-activation, $E_F$ in all doped samples shifts towards the $POPy_2$ LUMO level, while the conductivity of the films

remains at its intrinsic level; we attribute this behavior to an electron donation by a small fraction of the dimers to easily reduced deep electron traps, which raises $E_F$ of the system. This process, however, does not populate the low EA electron transport levels of the $POPy_2$ film (further discussion can be found in section 2.1 of the Supplementary Text). Following UV activation, $E_F$ moves further up in the gap and is pinned at about 2.6 eV below the vacuum level, or ~ 0.4 eV below the $POPy_2$ LUMO edge, while the conductivity increases by several orders of magnitude. Control experiments on undoped $POPy_2$ films show no significant change in WF or conductivity when UV-irradiated under the same conditions, and thus spurious effects related to UV-induced modifications of the host molecular film can be ruled out. Therefore, it is clear that in the doped samples, UV activation leads to a situation whereby electrons are transferred to lower EA unoccupied levels (shallow tail states and/or $POPy_2$ LUMO), resulting in a larger $E_F$ shift and an increase of the conductivity by several orders of magnitude.

The dynamic response of the WF and conductivity of doped $POPy_2$ during and after UV irradiation are shown in Table 1A and Fig. 2B, respectively. The dopant activation, as measured from the WF shift, is fast and nearly complete within a few seconds of irradiation. The initial increase in conductivity is fast as well, although complete saturation to a photo-equilibrium level under the experimental conditions used here takes a few hours. Following UV irradiation, the WF measured in the dark after several hours is found to be nearly unchanged. The conductivity shows a rapid but small decrease as the photoconductivity disappears when the UV irradiation is turned off, then slowly stabilizes to a slightly lower level, which is maintained for at least 15 weeks (Fig. S4). Therefore, both WF and conductivity measurements demonstrate the rapidity of the activation process and the high stability of the doped system.

To further probe the photo-assisted doping mechanism(s), activation was carried out with photon sources (Fig. S3), which emit at energies below the optical gap of both the host (3.1 eV) and the dopant in its dimer form (Fig. S2). Fig. 2C and Table 1B show the dynamic responses of the conductivity and WF of similarly doped $POPy_2$ films during and after deep red, green, blue, and UV irradiation. Note, however, that IR irradiation (940 nm) does not produce any noticeable increase in conductivity or decrease in work function (Fig. S5, Table S1). The initial increase in conductivity is fast for visible and UV photon energies, although saturation occurs notably more slowly with longer wavelength photons. Furthermore, seemingly saturated conductivity levels under deep red, green and blue irradiation, as well as post-irradiation stabilized levels in the dark, depend on the photon energy and remain significantly lower than for the UV-activated samples. Additional discussion on this point is given in Supplementary Information Section 2.2. Remarkably, stable conductivity was measured in one case for up to one year (Fig. 2C). Changes in WF follow the same trend.

Activation is required because of the low EA of the host relative to the IE of the $[RuCp^*Mes]_2$ dimer. The $[RuCp^*Mes]_2$ dimer has a relatively strong central C-C bond (Fig. 1D), but upon electron transfer to the host, the C-C bond in $[RuCp^*Mes]_2^+$ is greatly weakened and, undergoes rapid cleavage [27]. With $POPy_2$, this first electron transfer from the dimer to the host is a highly endergonic process ($\Delta G$ = +1.14 V from data in Fig. 1B and Fig. S6) and so is inhibited by an excessively large barrier. Therefore, the few dopants that do react without photo-activation are those that fill the low-density electron traps, causing an upward $E_F$ shift but no increase in conductivity. The highly endergonic electron transfer to shallow tail states and LUMO levels requires activation. This irradiation-assisted doping could in principle result (i) in the cleavage of the dimer excited state to form highly reducing monomers that can exergonically transfer an

electron to the host material, (ii) in electron transfer from the dimer excited state to the host, (iii) in electron transfer from the dimer to the host excited state, (iv) in dimer-to-host electron transfer through an intermolecular charge-transfer (CT) absorption, or (v) Förster resonance energy transfer (FRET) between different excited states. However, paths i, ii and v are negligible in the present case because of the very weak UV (375 nm) absorption in the dimers (Fig. S2). Absorption of UV photons takes place predominantly in the host, given its much greater absorptivity and concentration. Host-to-dimer FRET is forbidden by the lack of spectral overlap between $POPy_2$ PL and dimer absorption (Fig. S7). UV absorption in the host is, therefore, likely followed by process (iii) above (Fig. 3, top). Absorption of deep-red, green and blue photons, on the other hand, is only likely to happen by (iv) (Fig. 3, bottom); the presence of visible absorption attributable to a CT complex is confirmed by external quantum efficiency measurements of a solar cell ($EQE_{PV}$) comprised of a $[RuCp^*Mes]_2$-doped $POPy_2$ film (shown below).

Optical excitation at energies smaller than those of the molecular Frenkel absorption in the host or dimer can lead to photocurrent generation from the CT state, which is visualized through plots of the $EQE_{PV}$, measured on the device depicted in Supplementary Methods and Fig. S8. Fig. 4A shows one $EQE_{PV}$ scan of the undoped $POPy_2$ film, and two sequential $EQE_{PV}$ scans of the doped $POPy_2$ film (recorded from low (1.5 eV) to high energy (4.1 eV) for the first scan and reversed for the second scan). A broad low-energy feature ranging from 1.6 to 2.8 eV is evident in the first scan. We attribute this sub-bandgap feature to the CT state photocurrent generation mechanism (iv) above, because neither $POPy_2$, which defines the low-energy Frenkel absorption edge of this system, nor the dimer, absorb below 3.1 eV. The energy corresponding to the maximum of this visible band (ca. 2.1 eV) is also broadly consistent with that expected given the difference between the oxidation potential of the dimer and the reduction potential of the host (1.14 V) if one assumes a reorganization energy of ca. 1 eV for the dimer-to-host electron-transfer reaction (see discussion in Supporting Information). Upon scanning the device a second time, however, this CT state feature is no longer present. We propose that the probe beam during the first and second scans, especially in the high-energy region, quickly activate doping of the film, resulting in conversion of those dimers forming CT-complexes to monomer cations and leading to the elimination of the CT complex. In the inset figure, the probe beam photon energies are limited to the CT state absorption region and scanned repeatedly from low to high energy, leading to a progressive suppression of the CT state photocurrent generation, and confirming that photo-assisted activation with low energy photons occurs via CT state absorption.

Time-resolved EQE measurements yield a further analysis of the dynamics of activation with different irradiation. Fig. 4B and Table 1C show the evolution of the CT state absorption (indicative of the presence of dimer-form dopants) measured via photocurrent quickly probed at a reference photon energy of ~ 2.0 eV (620 nm) following irradiation of the sample with controlled doses of photons of various energies. It is found that UV light (3.3 eV) eliminates the CT state feature significantly faster than the red, green and blue light. The UV photon dose needed is also more than two orders of magnitude smaller than with any of the other three. This is attributed to the strong absorption of UV light in the host and dimer molecules, and the relatively weak oscillator strength for the presumed dimer-to-host CT transition.

The generality of the ability to photo-activate doping using $[RuCp^*Mes]_2$ to be extended beyond the thermodynamic doping strength was tested using three additional low electron affinity ETMs (all EAs measured via inverse photoemission spectroscopy): (i) tris(8-

hydroxyquinolinato)aluminum ($Alq_3$) (EA ~ 2.1 eV [36]); (ii) 2-[4-(9,10-Di-naphthalene-2-yl-anthracene-2-yl)-phenyl]-1-phenyl-1H-benzimidazole (ZADN) [37] (EA ~ 2.4 eV); (iii) contorted hexabenzocoronene (c-HBC) (EA = 2.2-2.5 eV [38,39]). All three exhibit WF and conductivity behavior very similar to $POPy_2$ (Fig. S9 and Table S2). Following photoactivation, the WF of the three compounds decreases, with $E_F$ pinned close to the LUMO level, while the conductivity increases by 4 to 6 orders of magnitude with respect to the undoped or non-activated sample. These results suggest that the n-doping of low EA organic semiconductors by $[RuCp^*Mes]_2$ in combination with UV irradiation is a general phenomenon.

Spatial confinement of dopants is critical to the stability of organic devices, which typically comprise stacks of doped and undoped layers. We used secondary ion mass spectrometry (SIMS) to investigate dopant diffusion across interfaces between undoped and doped $POPy_2$ layers (see Supplementary Methods and Fig. S10), as a function of device shelf-time and processing temperature. No detectable diffusion was observed, confirming the excellent spatial stability of the system.

To demonstrate the application of photo-activated n-doping, we fabricated an OLED using $Alq_3$ as the emitter and $POPy_2$ as the ETM (Fig. S11). Note that PEDOT:PSS (WF ~ 5.0 eV) was chosen here as the *electron-injection contact* for the purpose of demonstrating the power of doping in eliminating constraints on contact WF. The impact of $POPy_2$ doping and photo-activation is clearly depicted through the current density, luminance, and $EQE_{OLED}$ of the OLED in Fig. S11C & D. Due to the large PEDOT:PSS/$POPy_2$ electron-injection barrier, the undoped ETM injects a negligible electron current, yielding no measurable emission from the OLED. With doped and UV-activated $POPy_2$, the current density increases by two orders of magnitude, resulting in strong light emission. The $EQE_{OLED}$ of the UV-activated OLED also reaches the standard limit (~ 1%) of the $Alq_3$ emitter. Interestingly, OLEDs with doped, yet non-activated, $POPy_2$ become self-activated by the initially weak, although rapidly-increasing, internal light emission (details are shown in Fig. S12A & B), which is consistent with our finding that green light can (partially) activate doped films. Note that the same measurements performed on structures comprising a non-activated doped $POPy_2$ layer and no emissive layer show no sign of self-activation. Finally, as a further demonstration of this process, OLED pixels can become partially activated by the waveguided light emission from neighboring pixels (Fig. S12C & D).

The doped OLEDs were periodically tested over several weeks to investigate their long-term stability, which is critical for practical applications (Fig. S13). We find that the performance of the UV-activated OLEDs remains essentially unchanged after two weeks of storage in the dark under nitrogen atmosphere. Although the self-activated devices lose the effect of activation over time, they quickly recover under a new self-activation run. Finally, the application of this doping photo-activation process to high efficiency OLEDs is demonstrated by fabricating devices based on a doped $POPy_2$ ETL and a TPBI:$Ir(ppy)_3$ phosphorescent emission layer (Fig. 4A & B). These OLEDs achieve an 18% $EQE_{OLED}$ (Fig. 5C & D) without optimization and show good thermal stability (stable at 60 °C for 30 min; Fig. S14).

The combination of cleavable dimers, such as $[RuCp^*Mes]_2$, and photo-activation is therefore a promising avenue for efficient n-doping of very low EA materials, a range that was, thus far the domain of very reactive and diffusive elements such as alkali metals. These results suggest a new path to enable the mass production of highly conductive low-EA ETMs and the achievement of low electron-injection barriers regardless of the electrode WF, both of which are

255 required for high-energy emission OLEDs and other electronic and optoelectronic applications in
256 organic electronics.

**References:**


1. Lüssem, B., Riede, M. & Leo, K. Doping of organic semiconductors. *Phys. Status Solidi A Appl. Mater. Sci.* **210,** 9–43 (2013).
2. Salzmann, I. & Heimel, G. Toward a comprehensive understanding of molecular doping organic semiconductors (review). *J. Electron Spectros. Relat. Phenomena* **204,** 208–222 (2015).
3. Reineke, S. *et al.* White organic light-emitting diodes with fluorescent tube efficiency. *Nature* **459,** 234–239 (2009).
4. Murawski, C., Fuchs, C., Hofmann, S., Leo, K. & Gather, M. C. Alternative p-doped hole transport material for low operating voltage and high efficiency organic light-emitting diodes. *Appl. Phys. Lett.* **105,** 113303 (2014).
5. Selzer, F. *et al.* Improved organic p-i-n type solar cells with n-doped fluorinated hexaazatrinaphthylene derivatives HATNA-F6 and HATNA-F12 as transparent electron transport material. *J. Appl. Phys.* **115,** 54515 (2014).
6. Lei, X., Zhang, F., Song, T. & Sun, B. p-type doping effect on the performance of organic-inorganic hybrid solar cells. *Appl. Phys. Lett.* **99,** 233305 (2011).
7. Lüssem, B. *et al.* Doped organic transistors operating in the inversion and depletion regime. *Nat. Commun.* **4,** 2775 (2013).
8. Ma, L. *et al.* High performance polythiophene thin-film transistors doped with very small amounts of an electron acceptor. *Appl. Phys. Lett.* **92,** 63310 (2008).
9. Naab, B. D. *et al.* High Mobility N-Type Transistors Based on Solution- Sheared Doped 6,13-Bis(triisopropylsilylethynyl)pentacene Thin Films. *Adv. Mater.* **25,** 4663–4667 (2013).
10. Olthof, S. *et al.* Passivation of trap states in unpurified and purified C60 and the influence on organic field-effect transistor performance. *Appl. Phys. Lett.* **101,** 253303 (2012).
11. Oh, J. H., Wei, P. & Bao, Z. Molecular n-type doping for air-stable electron transport in vacuum-processed n-channel organic transistors. *Appl. Phys. Lett.* **97,** 243305 (2010).
12. Tang, C. G. *et al.* Doped polymer semiconductors with ultrahigh and ultralow work functions for ohmic contacts. *Nature* **539,** 536–540 (2016).
13. Kulkarni, A. P., Tonzola, C. J., Babel, A. & Jenekhe, S. A. Electron Transport Materials for Organic Light-Emitting Diodes. *Chem. Mater.* **16,** 4556–4573 (2004).
14. Chan, C. K., Kim, E. G., Brédas, J.-L. & Kahn, A. Molecular n-Type Doping of 1,4,5,8-Naphthalene Tetracarboxylic Dianhydride by Pyronin B Studied Using Direct and Inverse Photoelectron Spectroscopies. *Adv. Funct. Mater.* **16,** 831–837 (2006).
15. Werner, A. G. *et al.* Pyronin B as a donor for n-type doping of organic thin films. *Appl. Phys. Lett.* **82,** 4495–4497 (2003).
16. Li, F., Werner, A., Pfeiffer, M., Leo, K. & Liu, X. Leuco Crystal Violet as a Dopant for n-Doping of Organic Thin Films of Fullerene C60. *J. Phys. Chem. B* **108,** 17076–17082 (2004).

17. Li, F. *et al.* Acridine orange base as a dopant for n doping of C60 thin films. *J. Appl. Phys.* **100,** 1–9 (2006).

18. Wei, P. *et al.* 2-(2-Methoxyphenyl)-1,3-dimethyl-1H-benzoimidazol-3-ium Iodide as a New Air-Stable n-Type Dopant for Vacuum-Processed Organic Semiconductor Thin Films. *J. Am. Chem. Soc.* **134,** 3999–4002 (2012).

19. Wei, P., Oh, J. H., Dong, G. & Bao, Z. Use of a 1H-Benzoimidazole Derivative as an n-Type Dopant and To Enable Air-Stable Solution-Processed n-Channel Organic Thin-Film Transistors. *J. Am. Chem. Soc.* **132,** 8852–8853 (2010).

20. Schlitz, R. A. *et al.* Solubility-Limited Extrinsic n-Type Doping of a High Electron Mobility Polymer for Thermoelectric Applications. *Adv. Mater.* **26,** 2825–2830 (2014).

21. Naab, B. D. *et al.* Effective Solution- and Vacuum-Processed n-Doping by Dimers of Benzimidazoline Radicals. *Adv. Mater.* **26,** 4268–4272 (2014).

22. Rossbauer, S., Müller, C. & Anthopoulos, T. D. Comparative Study of the N-Type Doping Efficiency in Solution-processed Fullerenes and Fullerene Derivatives. *Adv. Funct. Mater.* **24,** 7116–7124 (2014).

23. Naab, B. D. *et al.* Mechanistic Study on the Solution-Phase n-Doping of 1,3-Dimethyl-2-aryl-2,3-dihydro-1H-benzoimidazole Derivatives. *J. Am. Chem. Soc.* **135,** 15018–15025 (2013).

24. Zhang, Y., de Boer, B. & Blom, P. W. M. Trap-free electron transport in poly( p -phenylene vinylene) by deactivation of traps with n -type doping. *Phys. Rev. B* **81,** 85201 (2010).

25. Weber, C. D., Bradley, C. & Lonergan, M. C. Solution phase n-doping of C 60 and PCBM using tetrabutylammonium fluoride. *J. Mater. Chem. A* **2,** 303–307 (2014).

26. Guo, S. *et al.* n-Doping of Organic Electronic Materials using Air-Stable Organometallics. *Adv. Mater.* **24,** 699–703 (2012).

27. Guo, S. *et al.* n-Doping of Organic Electronic Materials Using Air-Stable Organometallics: A Mechanistic Study of Reduction by Dimeric Sandwich Compounds. *Chem. - A Eur. J.* **18,** 14760–14772 (2012).

28. Qi, Y. *et al.* Solution doping of organic semiconductors using air-stable n-dopants. *Appl. Phys. Lett.* **100,** 83305 (2012).

29. Olthof, S. *et al.* Ultralow Doping in Organic Semiconductors: Evidence of Trap Filling. *Phys. Rev. Lett.* **109,** 176601 (2012).

30. Higgins, A., Mohapatra, S. K., Barlow, S., Marder, S. R. & Kahn, A. Dopant controlled trap-filling and conductivity enhancement in an electron-transport polymer. *Appl. Phys. Lett.* **106,** 163301 (2015).

31. Mohapatra, S. K. *et al.* Dimers of Nineteen-Electron Sandwich Compounds: Crystal and Electronic Structures, and Comparison of Reducing Strengths. *Chem. - A Eur. J.* **20,** 15385–15394 (2014).

32. Walzer, K., Maennig, B., Pfeiffer, M. & Leo, K. Highly efficient organic devices based on electrically doped transport layers. *Chem. Rev.* **107,** 1233–71 (2007).

33. Oyamada, T. *et al.* Extremely low-voltage driving of organic light-emitting diodes with a Cs-doped phenyldipyrenylphosphine oxide layer as an electron-injection layer. *Appl. Phys. Lett.* **86,** 33503 (2005).

34. Matsushima, T. & Adachi, C. High-current Injection and Transport on Order of kA/cm2 in Organic Light-emitting Diodes Having Mixed Organic/Organic Heterojunction Interfaces. *Jpn. J. Appl. Phys.* **46,** L861–L863 (2007).

35. Matsushima, T. & Adachi, C. Suppression of exciton annihilation at high current densities in organic light-emitting diode resulting from energy-level alignments of carrier transport layers. *Appl. Phys. Lett.* **92,** 63306 (2008).

36. Yoshida, H. & Yoshizaki, K. Electron affinities of organic materials used for organic light-emitting diodes: A low-energy inverse photoemission study. *Org. Electron.* **20,** 24–30 (2015).

37. Choi, J. M. & Lee, J. Y. Triplet emitter doped exciton harvesting layer for improved efficiency and long lifetime in blue phosphorescent organic light-emitting diodes. *Synth. Met.* **220,** 573–577 (2016).

38. Hiszpanski, A. M. *et al.* Halogenation of a nonplanar molecular semiconductor to tune energy levels and bandgaps for electron transport. *Chem. Mater.* **27,** 1892–1900 (2015).

39. Davy, N. C. *et al.* Contorted Hexabenzocoronenes with Extended Heterocyclic Moieties Improve Visible-Light Absorption and Performance in Organic Solar Cells. *Chem. Mater.* **28,** 673–681 (2016).

40. Pommerehne, J. *et al.* Efficient Two Layer LEDs on a Polymer Blend Basis. *Adv. Mater.* **7,** 551–554 (1995).

41. Tao, Y. T., Balasubramaniam, E., Danel, A. & Tomasik, P. Dipyrazolopyridine derivatives as bright blue electroluminescent materials. *Appl. Phys. Lett.* **77,** 933 (2000).

42. Swensen, J. S. *et al.* Improved Efficiency in Blue Phosphorescent Organic Light-Emitting Devices Using Host Materials of Lower Triplet Energy than the Phosphorescent Blue Emitter. *Adv. Funct. Mater.* **21,** 3250–3258 (2011).

43. Hill, I. G., Kahn, A., Soos, Z. G. & Pascal, Jr, R. A. Charge-separation energy in films of π-conjugated organic molecules. *Chem. Phys. Lett.* **327,** 181–188 (2000).

44. Kahn, A., Koch, N. & Gao, W. Electronic structure and electrical properties of interfaces between metals and π-conjugated molecular films. *J. Polym. Sci. Part B Polym. Phys.* **41,** 2529–2548 (2003).

45. Wu, C. I., Hirose, Y., Sirringhaus, H. & Kahn, A. Electron-hole interaction energy in the organic molecular semiconductor PTCDA. *Chem. Phys. Lett.* **272,** 43–47 (1997).

46. Vandewal, K. *et al.* Absorption Tails of Donor:C 60 Blends Provide Insight into Thermally Activated Charge-Transfer Processes and Polaron Relaxation. *J. Am. Chem. Soc.* **139,** 1699–1704 (2017).

47. Zhan, X. *et al.* Electron Affinities of 1,1-Diaryl-2,3,4,5-tetraphenylsiloles: Direct Measurements and Comparison with Experimental and Theoretical Estimates. *J. Am. Chem. Soc.* **127,** 9021–9029 (2005).

**Acknowledgments:** A.K., X.L. and F.Z. acknowledge funding for this work from the National Science Foundation under grants DMR-1506097. Work in Berlin was supported by the Sfb951 (DFG) and the Helmholtz Energy-Alliance "Hybrid Photovoltaics". B.P.R., M.A.F., and K.M.L. acknowledge funding for this work from the Department of Energy EERE SSL Program under Award #DE-EE0006672 and the Office of Basic Energy Sciences, Division of Materials Sciences and Engineering under Award #DE-SC0012458. Work at the Georgia Institute of Technology was supported by the National Science Foundation under grants DMR-1305247. We thank Elena Longhi for synthetic assistance, Prof. Emil List-Kratochvil for stimulating discussions about optical interference phenomena during UV/Vis measurements, Dr. Giovanni Ligorio for perfoming PL measurements in Berlin and Dr. Anton Zykov, Dr. Peter Schäfer and Prof. Stefan Kowarik for performing XRD measurements.

**Author Contributions:** X.L., B.W., K.M., A.K., N.K., S.R.M. and S.B. initialized this series of experiments. K.M, S.B. and S.R.M. synthesized the dopant molecules. X.L., B.W., A.K. and N.K. designed the work function and conductivity experiments, prepared the films, and carried out Kelvin probe, *I-V*, AFM, UPS, XPS and IPES measurements. B.W. and N.K. conducted optical absorption spectroscopy. K.M.L and B.P.R. performed part of PL experiments in Princeton. X.L., K.M.L., M.A.F., B.P.R. and A.K. designed and performed $EQE_{PV}$ and OLED measurements. F.Z, K.M.L, X.L. and A.K. designed and fabricated samples for SIMS and RBS. All authors discussed the results and contributed to the manuscript.

**Competing financial interests:** The authors declare no competing financial interests.

**Materials & Correspondence:** Correspondence and material requests should be addressed to A.K.

## Figures:

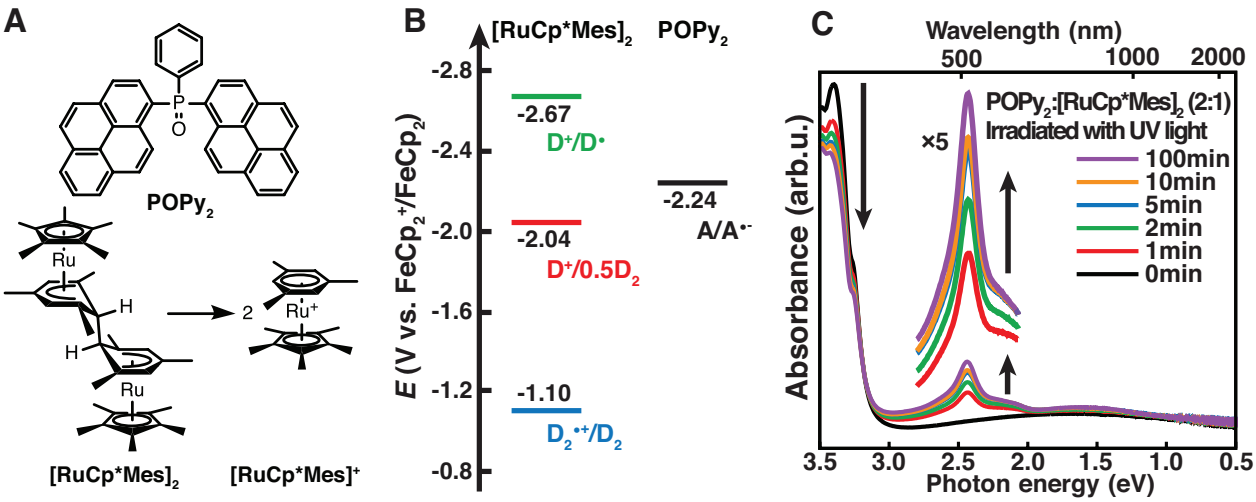


**D**

| | | | |
|---|---|---|---|
| (a) | $[RuCp^*Mes]^\bullet + POPy_2 \rightarrow [RuCp^*Mes]^+ + POPy_2^{\bullet-}$ | $\Delta G$ = - 0.43 eV |
| (b) | $[RuCp^*Mes]_2 + POPy_2 \rightarrow [RuCp^*Mes]_2^{\bullet+} + POPy_2^{\bullet-}$ | $\Delta G$ = + 1.14 eV |
| (c) | $[RuCp^*Mes]_2 \rightarrow 2\,[RuCp^*Mes]^\bullet$ | $\Delta G$ = + 1.26 eV |
| (d) | $[RuCp^*Mes]_2 + 2\,POPy_2 \rightarrow 2\,[RuCp^*Mes]^+ + 2\,POPy_2^{\bullet-}$ | $\Delta G$ = + 0.40 eV |

**Fig. 1. (A)** Chemical structures of the host material $POPy_2$ (A) and the dimeric dopant $[RuCp^*Mes]_2$ ($D_2$) with associated cationic monomer; **(B)** Electrochemical redox-potentials of the host and the dopant measured by CV in THF vs. ferrocenium/ferrocene ($FeCp_2^+/FeCp_2$). CV revealed the $D^+/D^\bullet$ monomer at -2.67 V vs. $FeCp_2^+/FeCp_2$, which is ca. 1.6 V more anodic than the $D_2^{\bullet+}/D_2$ potential (-1.1 V vs. $FeCp_2^+/FeCp_2$), consistent with the good reducing ability of the monomer and the moderate air-stability of the dimer. The effective reducing strength of $[RuCp^*Mes]_2$, the $D^+/0.5D_2$ potential, estimated by Mohapatra et al. [31] to be around -2.04 V vs. $FeCp_2^+/FeCp_2$, constitutes the thermodynamic limit for successful n-doping, implying that the dimers are only able to n-dope materials with reduction potentials more cathodic than this value or, equivalently, EAs higher than ca. 2.8 eV (estimated using the standard method of adding 4.8 eV as the potential of $FeCp_2^+/FeCp_2$ vs. vacuum [40]); **(C)** Optical absorption spectra of UV-activated thin films of $POPy_2$ doped with $[RuCp^*Mes]_2$, as a function of UV irradiation time. The molar ratio $POPy_2$:$[RuCp^*Mes]_2$ is about 33%, which corresponds to 4.6 for the Ru/O ratio used below. The broad feature centered at 1.6 eV is an artifact, due to optical interference within the thin $POPy_2$ film, as shown in Fig. S2. **(D)** Estimated free energies (from data summarized in **(B)** for some possible reactions involving RuCp*Mes species and $POPy_2$. (a) indicates that reaction of the $[RuCp^*Mes]^\bullet$ monomer and $POPy_2$ is expected to be exergonic. However, electron-transfer from dimer to $POPy_2$ (b) and cleavage of the dimer (c), which would be possible first steps for reaction in the dark, are both highly endergonic. Moreover, the overall reaction of the dimer and $POPy_2$, (d), is expected to be endergonic, and, therefore, the doped state to be thermodynamically unfavorable ($\bullet$ refers to species with unpaired electron and * refers to excited species).

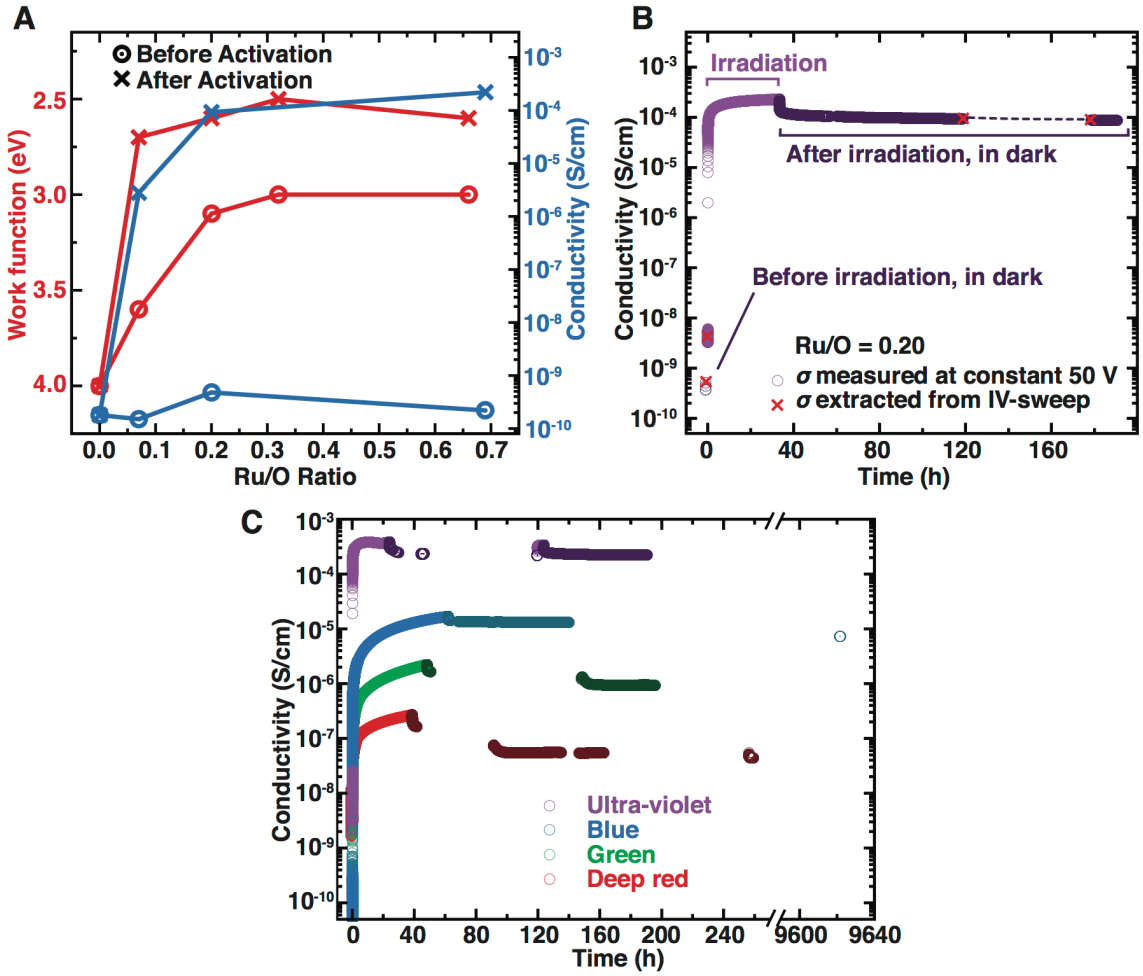


**Fig. 2. (A)** WF (red) and conductivity (blue) of the $POPy_2$ film as a function of doping concentration (Ru/O ratio), before and after UV activation**; (B)** Conductivity ($\sigma$) of a typical doped $POPy_2$ film as a function of time, before, during and after UV irradiation; **(C)** Conductivity of doped $POPy_2$ films as a function of time, during and after irradiation with photons of different wavelengths (375, 470, 530, and 660 nm). The brighter part of each curve corresponds to conductivity under irradiation, while the darker part represents conductivity following irradiation. Post-photo-activation conductivity shows excellent stability, measured over hundred of hours (and up to more than a year in one case).

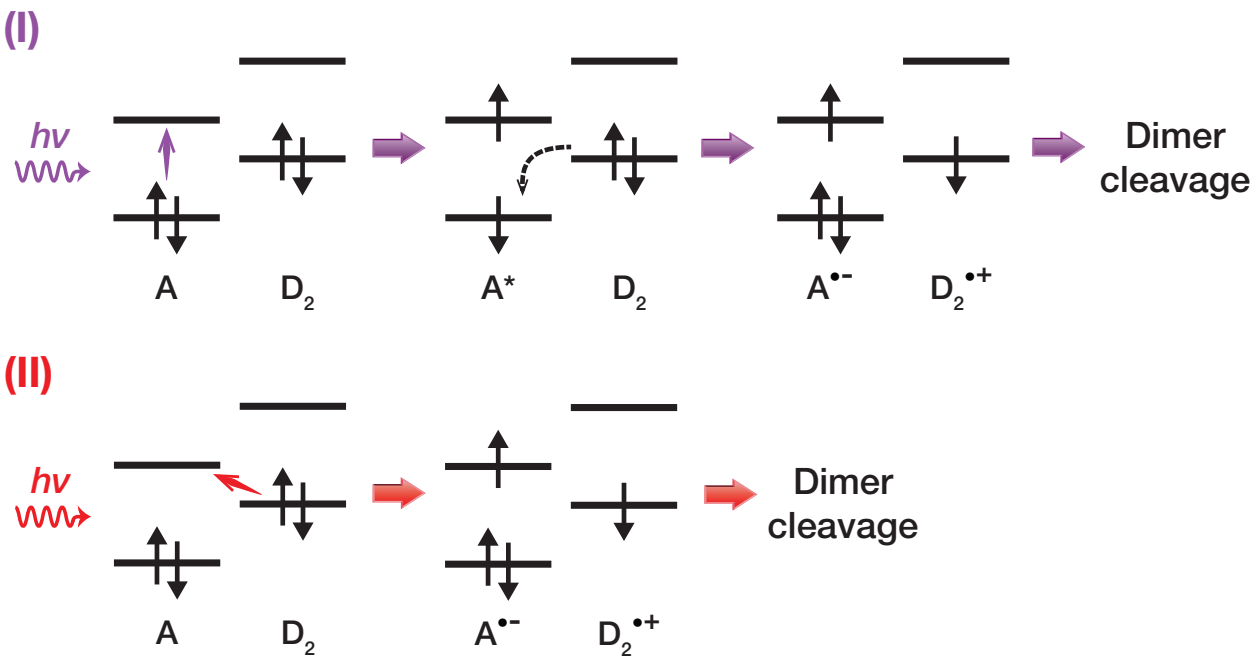


**Fig. 3.** Dominant paths for the photo-assisted doping for the dimer/host system. (I) electron transfer from the dimer to the host excited state, followed by cleavage of the cation dimer; (II) dimer-to-host electron transfer through an intermolecular charge-transfer (CT) absorption, followed by cleavage of the cation dimer (• refers to species with unpaired electron and * refers to excited species). In these reactions, A stands for the host (acceptor) and D for the dopant.

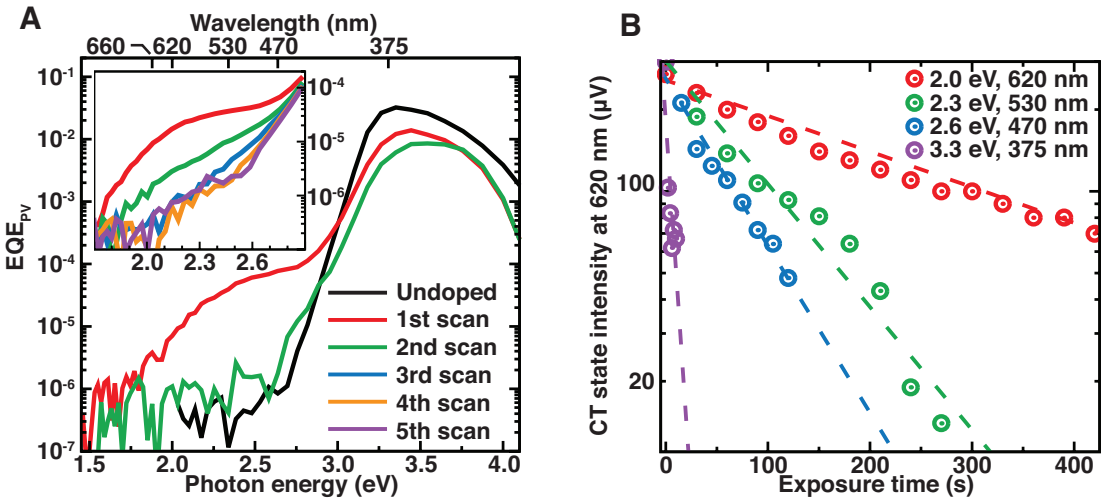


**Fig. 4.** **(A)** One $EQE_{PV}$ scan of the undoped $POPy_2$ film and two sequential $EQE_{PV}$ scans of the doped $POPy_2$ film (Ru/O ~ 1.4, recorded from low (1.5 eV) to high energy (4.1 eV) for the first scan and reversed for the second scan); Inset: five sequential $EQE_{PV}$ scans taken from low to high energy within the CT state spectral region of another doped $POPy_2$ film; both show the progressive disappearance of the CT state signal; **(B)** Time evolution of the CT state spectral signal under different photo-activation energies.

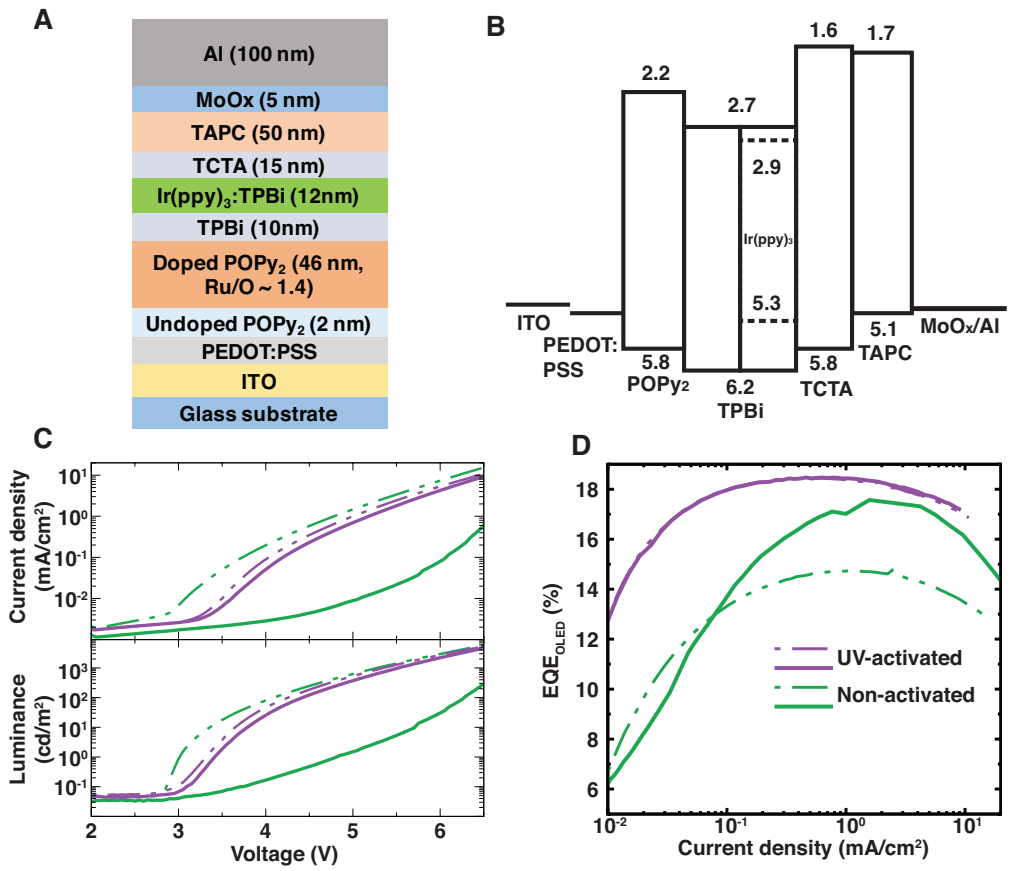


**Fig. 5. (A) and (B):** Structure and energy diagram of an OLED using TPBi:Ir(ppy)$_3$ as the green emitter layer. The electronic structures of TPBi, Ir(ppy)$_3$, TCTA, and TAPC are from ref.[41], [36], [36], and [42], respectively. The 2 nm undoped $POPy_2$ layer serves as a simple buffer that prevents co-evaporated dopants from reaching the PEDOT:PSS surface and changing its work function. **(C)** Current density, luminance vs. voltage and **(D)** $EQE_{OLED}$ vs. current density of the TPBi:Ir(ppy)$_3$ OLEDs. Green and magenta curves correspond to OLEDs with non-activated and UV-activated doped $POPy_2$ layers, respectively. In each category, the full curve corresponds to the first scan, and the dot-dashed curve corresponds to the 10$^{th}$ scan (and shows self-activated doping). The large difference between 1$^{st}$ and 10$^{th}$ scans for the doped but non-activated device reflects the self-activation discussed in the text.

**Table 1.** **(A)** Evolution of the WF and conductivity of $POPy_2$ films as a function of $[RuCp^*Mes]_2$ concentration, before and after UV activation. The Ru/O ratio is given as an indication for the doping concentration; **(B)** Evolution of the WF of $POPy_2$ films as a function of $[RuCp^*Mes]_2$ concentration, before and after activation with different photon energies. The Ru/O ratio is given as an indication of the doping concentration**; (C)** Dynamics of decay of CT state at various irradiation wavelengths.

**(A)**

| Ru/O ratio | | 0.00 [a] | 0.07 | 0.20 | 0.32 | 0.66 | 0.69 |
|---|---|---|---|---|---|---|---|
| Work function (eV) | Before activation | 4.0 | 3.6 | 3.1 | 3.0 | 3.0 | -- |
| | 2 s UV | -- | 2.6 | 2.6 | 2.5 | 2.6 | -- |
| | 5 min UV | 4.1 | 2.6 | 2.6 | 2.4 | 2.5 | -- |
| | Few hours in dark [b] | 4.0 (3) | 2.7 (48) | 2.6 (59) | 2.5 (43) | 2.6 (13) | -- |
| Conductivity (S/cm) | Before activation | $1.8\times10^{-10}$ | $1.5\times10^{-10}$ | $4.8\times10^{-10}$ | -- | -- | $2.2\times10^{-10}$ |
| | After activation | $2.1\times10^{-10}$ | $2.8\times10^{-6}$ | $9.3\times10^{-5}$ | -- | -- | $2.2\times10^{-4}$ |

[a] Pristine $POPy_2$.
[b] Number of hours is listed in parentheses.

**(B)**

| Irradiation | | Deep red (660 nm) | Green (530 nm) | Blue (470 nm) | Ultra-violet (375 nm) |
|---|---|---|---|---|---|
| Work function (eV) | Before activation | 3.4 | 3.4 | 3.5 | 3.0 |
| | 2s activation | 3.4 | 3.1 | 2.8 | 2.6 |
| | 5 min activation | 2.8 | 2.6 | 2.5 | 2.5 |
| | 20 min activation | 2.6 | 2.7 | 2.5 | N/A |
| | Few hours in dark [a] | 2.7 (50) | 2.8 (74) | 2.5 (68) | 2.6 (13) |
| | | 3.0 (+88) | 3.1 (+70) | 2.5 (+75) | N/A |
| | | 3.0 (+116) | 3.1 (+6) | 2.5 (+144) | N/A |
| Ru/O ratio [b] | | 1.42 | 1.11 | 0.76 | 0.66 |

[a] Number of hours is listed in parentheses; "+" means additional hours.
[b] The variance of Ru/O ratio has negligible impact.

**(C)**

| Irradiation wavelength (nm) | | 620 | 530 | 470 | 375 |
|---|---|---|---|---|---|
| Photon energy (eV) | | 2.0 | 2.3 | 2.6 | 3.3 |
| Decay by 1/e | Time (s) | 290±15 | 92±15 | 58±6 | 3±1 |
| | # of photons | $(7.5\pm0.4)\times10^{14}$ | $(2.2\pm0.4)\times10^{14}$ | $(9.5\pm1.0)\times10^{13}$ | $(1.4\pm0.6)\times10^{12}$ |
| | Energy (J) | $(2.4\pm0.1)\times10^{-4}$ | $(8.2\pm0.1)\times10^{-5}$ | $(4.0\pm0.4)\times10^{-5}$ | $(7.4\pm3.3)\times10^{-7}$ |

**Extended Data:**

Figures S1-S15

Tables S1-S3

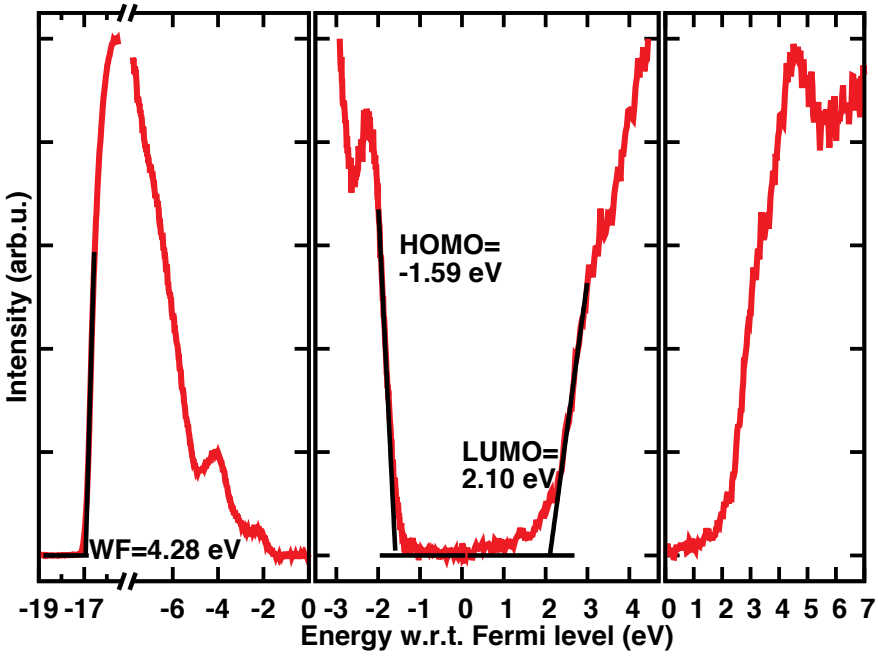


**Fig. S1**

(Left panel) photoemission cut-off and occupied states of $POPy_2$ measured by ultraviolet photoemission spectroscopy (UPS) (HeI); (Right panel) unoccupied states measured by inverse photoemission spectroscopy (IPES); (Center panel) expanded view of the $POPy_2$ gap, showing the top of the HOMO and the bottom of the LUMO. The 0 eV reference energy corresponds to the Fermi level, $E_F$, independently measured on a metallic surface in electrical contact with the sample. The UPS data indicate a film WF = 4.28 eV and IE = 5.87 eV, the latter in good agreement with the 5.9 eV obtained by Matsushima et al. [35]. The IPES spectrum is more difficult to analyze in view of the tail of states that extends below the lowest unoccupied molecular orbital (LUMO) of $POPy_2$ and of the sensitivity of the material to electron irradiation. The linear extrapolation of the leading edge of the IPES spectrum yields an EA equal to 2.2 eV. This low value is in line with that found for other typical ETMs used in OLEDs, for example $Alq_3$ [36,43] (and a little lower than the value of 2.46 eV that would be obtained from its solution reduction potential of –2.24 V vs. $FeCp_2^+/FeCp_2$ assuming a 4.8 eV offset). The resulting single-particle gap defined by IE – EA is 3.7 eV, which is ca. 0.6 eV larger than the optical gap defined by the onset of optical absorption at 3.1 eV (Fig. S2), the difference being attributable to the substantial exciton-binding energy expected for a small molecule like $POPy_2$. UPS and IPES were also performed on pristine $POPy_2$ thin films deposited on indium tin oxide (data not shown here) instead of PEDOT:PSS and produced very similar results.

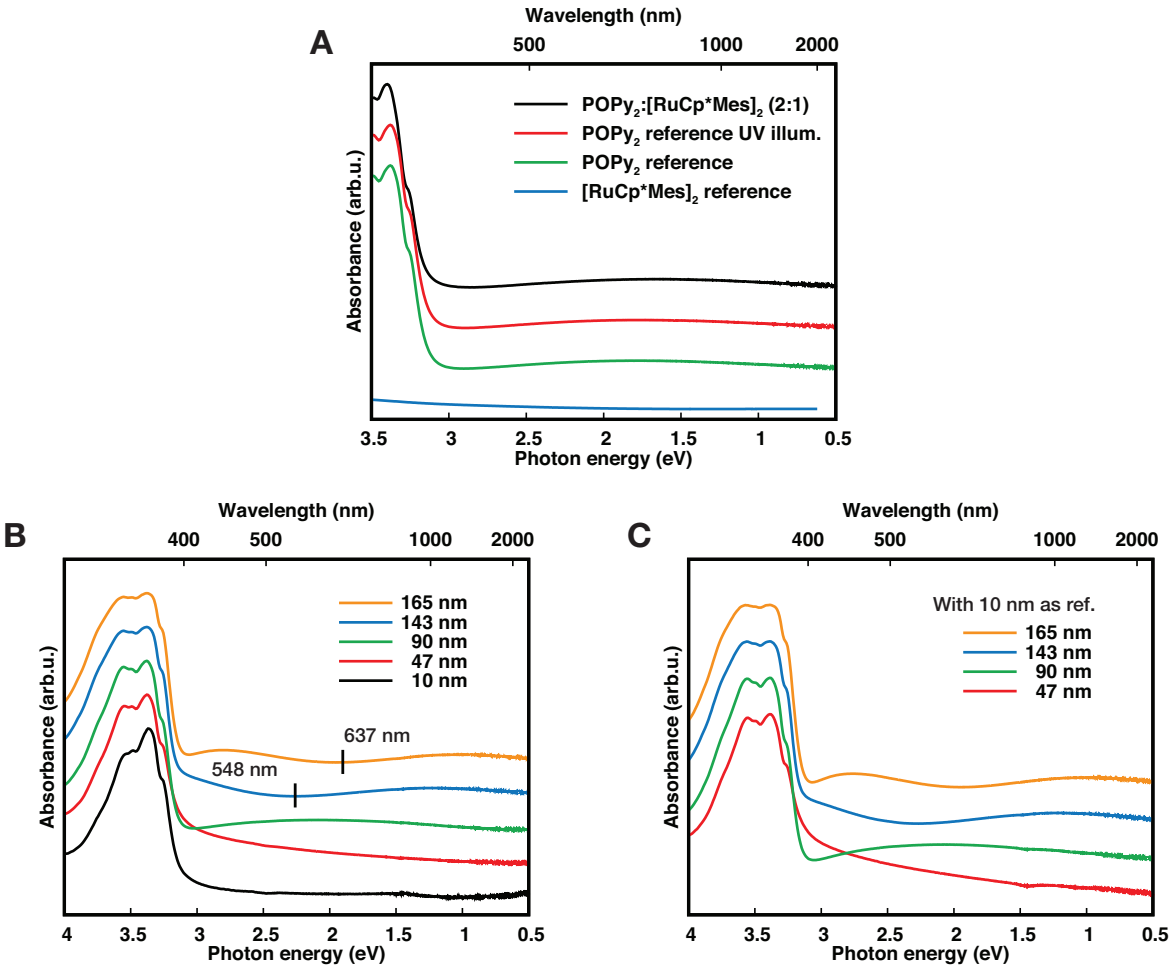


**Fig. S2**

**(A)** Optical absorption spectra of 100 nm doped and undoped $POPy_2$, and $[RuCp^*Mes]_2$ films. The spectrum of the non-activated doped $POPy_2$ film (black) shows the same features as the undoped $POPy_2$ film (green). The main feature at 3.4 eV is attributed to neutral $POPy_2$. Additionally, the spectrum of the undoped $POPy_2$ film following a 10 min UV illumination (red) is identical to the one non-activated. Therefore, the UV illumination used in this work does not lead to any significant change in the optical features of the $POPy_2$ host. The optical gap of the undoped host is 3.1 eV, while $[RuCp^*Mes]_2$ starts to absorb weakly at 3.1 eV. As in Fig. 1C, the broad feature centered at 1.6 eV is an artifact, due to optical interference within the thin $POPy_2$ film. **(B)** Optical absorption measurements on $POPy_2$ films with different thicknesses ranging from 10 to 165 nm; **(C)** Double-beam absorption measurement with a 10 nm thick sample used as a reference. The broad feature centered at 1.6 eV seen in Figs. 1C and S2 stems from interference within the thin $POPy_2$ film following the known relationship $2d = (k+1/2)\lambda$ with k = 0,1,… , d the thickness of the film and $\lambda$ the wavelength of the probing light. This interference effect leads to an enhanced transmission, and therefore various dips in the absorbance spectra, at specific wavelengths, as can be seen clearly in the absorption spectra of the 143 nm and 165 nm thick films. This contribution leads to an artifact in films with thickness around 100 nm, which has a similar appearance to a broad sub-band gap absorption feature.

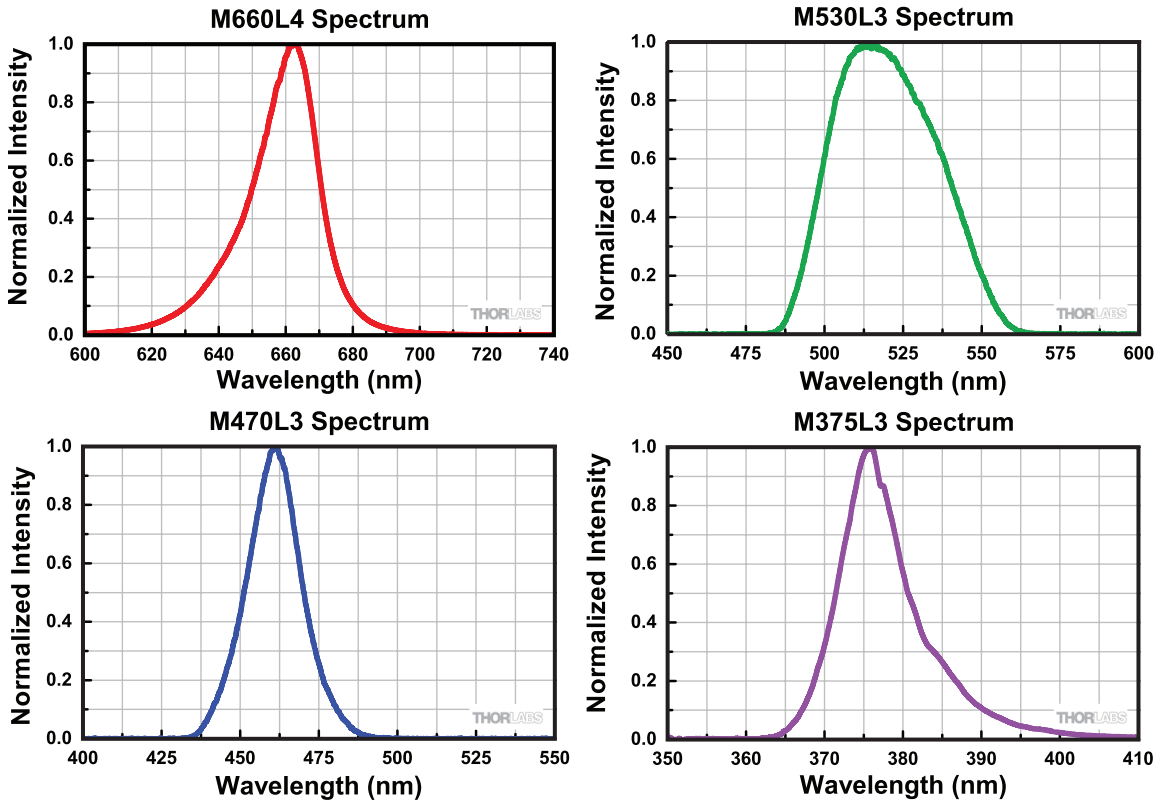


**Fig. S3**

Emission spectra of the four activation sources (deep-red, green, blue and ultra-violet) used in this study. Reprinted from Thorlabs Inc. with permission.

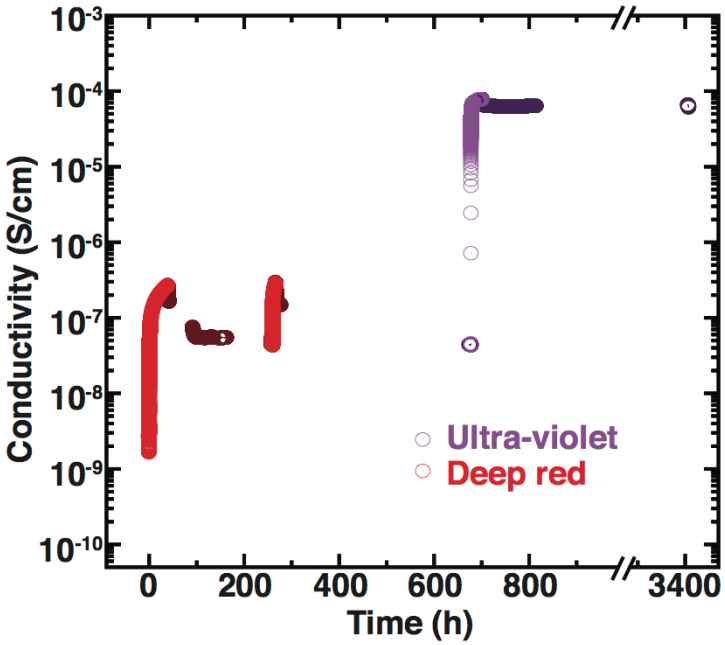


**Fig. S4**

Conductivity of a doped $POPy_2$ film (Ru/O = 1.42) sequentially photo-activated using the deep red, and UV sources.

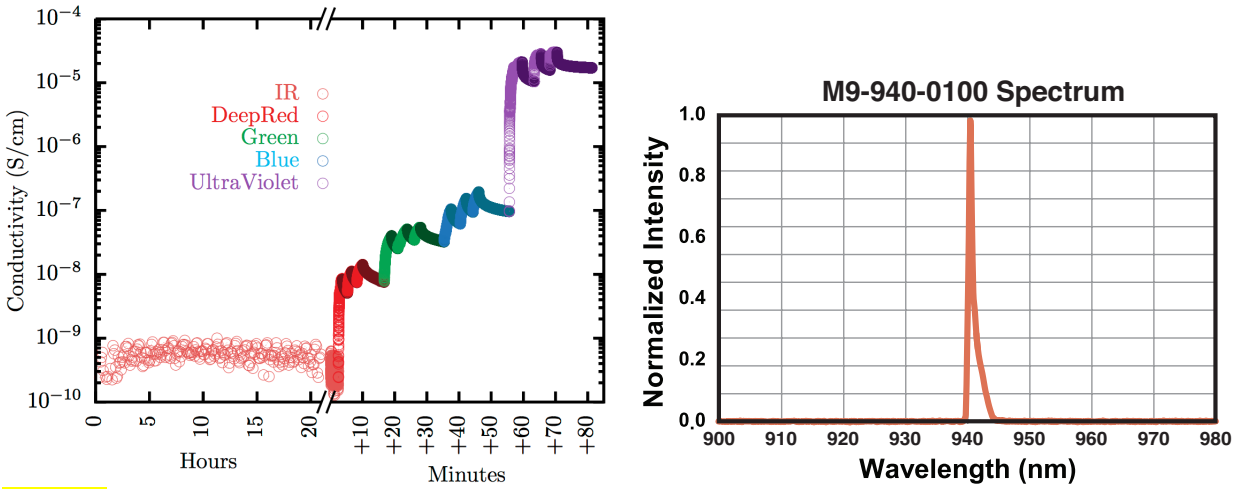


**Fig. S5:**

Conductivity (left) of a doped $POPy_2$ film (Ru/O = 0.86) photo-activated using the IR source (right, 940 nm, reprinted from Thorlabs Inc. with permission.) for several hours, followed by short illumination periods with the deep red, green, blue and UV sources. The initial IR illumination does not activate doping, the photon energy (1.3 eV) being too small to lead to CT state absorption.

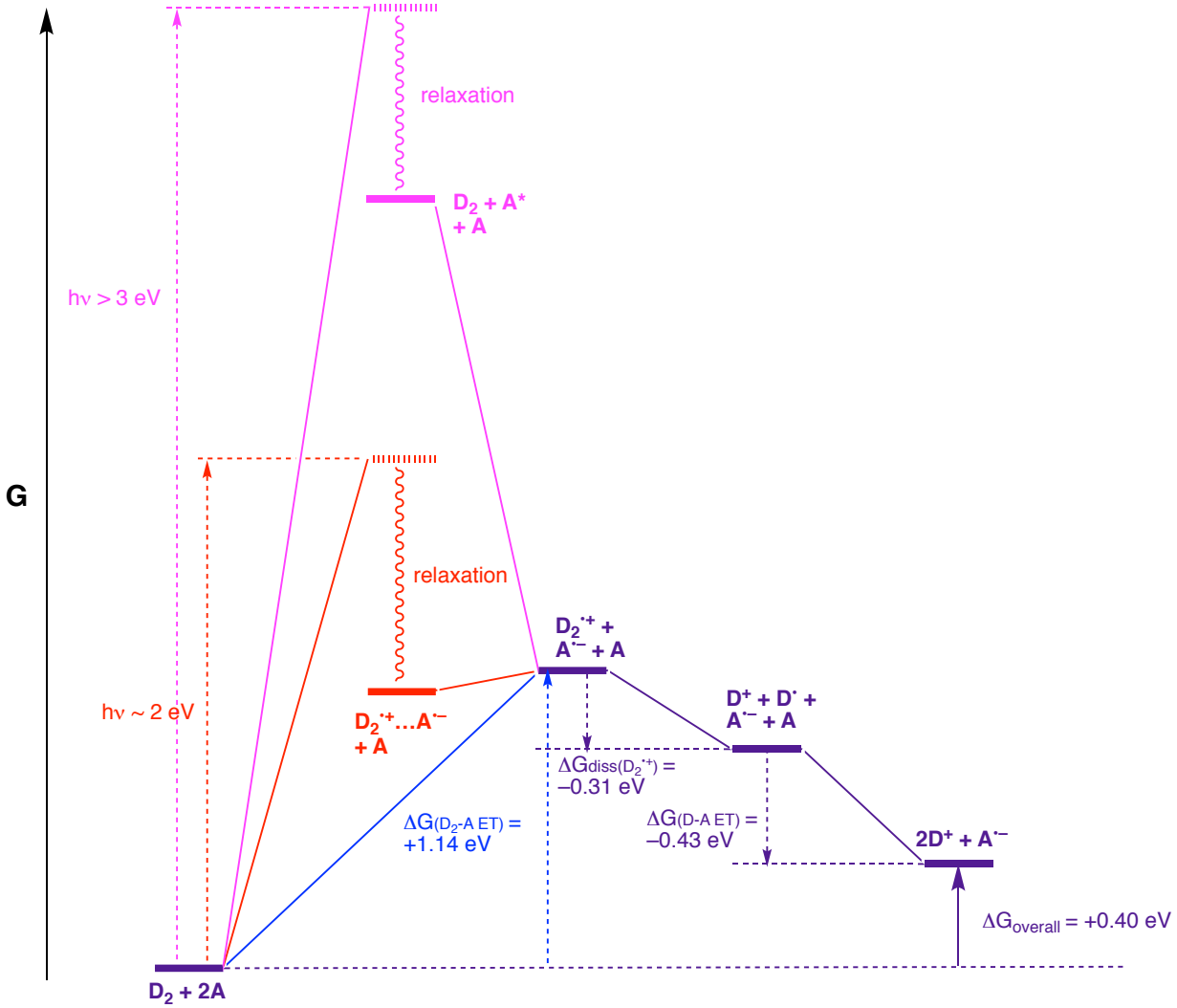


**Fig. S6:**

Pathways and estimated energetics for thermal and photodoping of $POPy_2$ (A) with $[RuCp^*Mes]_2$ ($D_2$). Intermediates: bold horizontal lines. Non-relaxed photoexcited species: horizontal hashed lines. Pathways: solid lines. Energies: arrows, with horizontal dotted lines for additional clarity as to which species are involved. The thermal pathway is shown in blue and is not feasible given the highly endergonic initial step; pathways through UV and red excitation are shown in red and magenta, respectively; and species and processes common to all mechanisms are shown in dark purple.

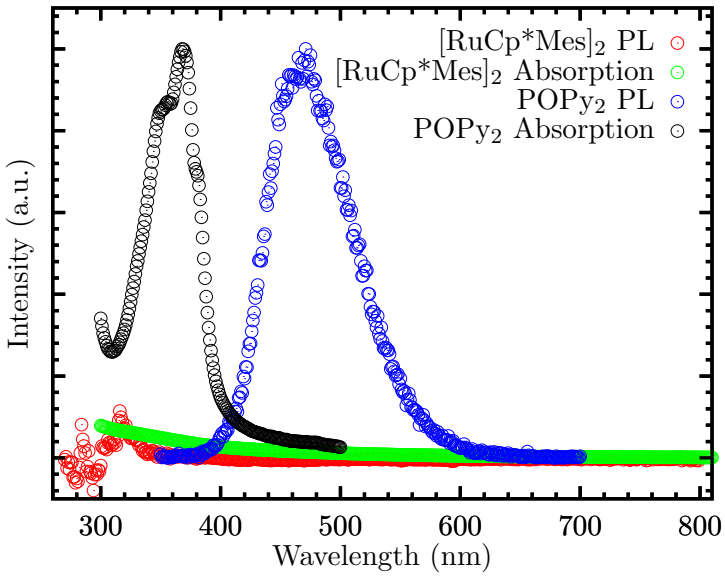


**Fig. S7:**

Absorption and photoluminescence measured on the host $POPy_2$ and the dimer $[RuCp^*Mes]_2$. The absence of significant dimer absorption and PL in the range of wavelengths considered here precludes FRET between host and dimer.

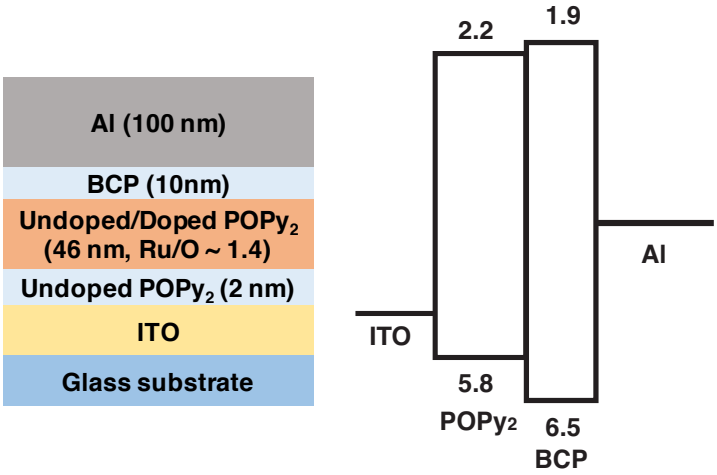


**Fig. S8:**
Structure and energy diagram for $EQE_{PV}$ test. EA and IE of BCP are from ref.[36].

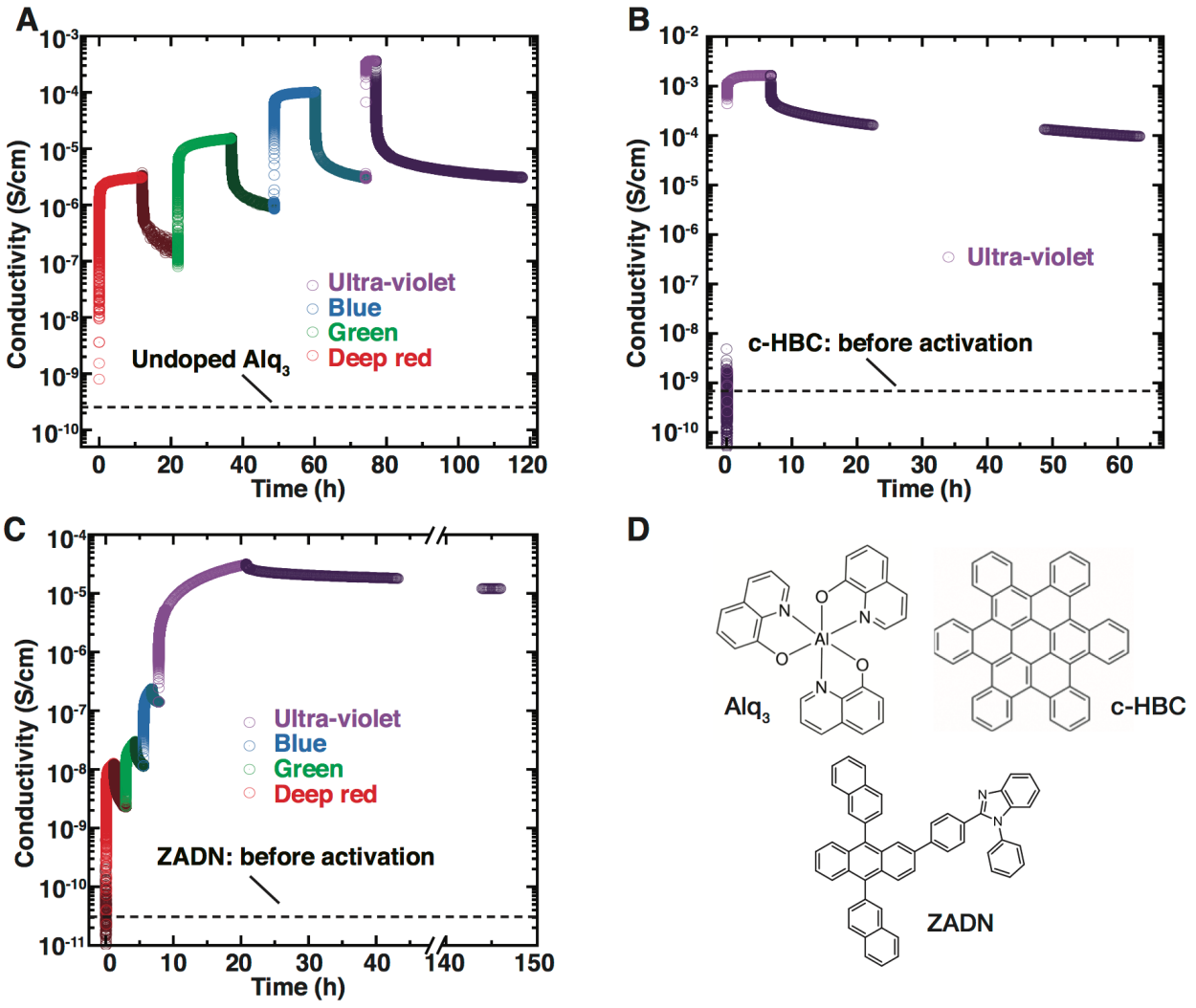


**Fig. S9:**

Conductivity of a doped **(A)** $Alq_3$ film (Ru/(1/3O) = 0.27), **(B)** c-HBC film (dopant concentration equivalent that of $POPy_2$ (Ru/O = 0.40), and **(C)** ZADN film (Ru/(1/2N) = 1.17) sequentially photo-activated using different sources. The horizontal dashed line corresponds to the conductivity of the undoped film (A) or the non-activated doped film (B and C). **(D)** Chemical structures of the three compounds.

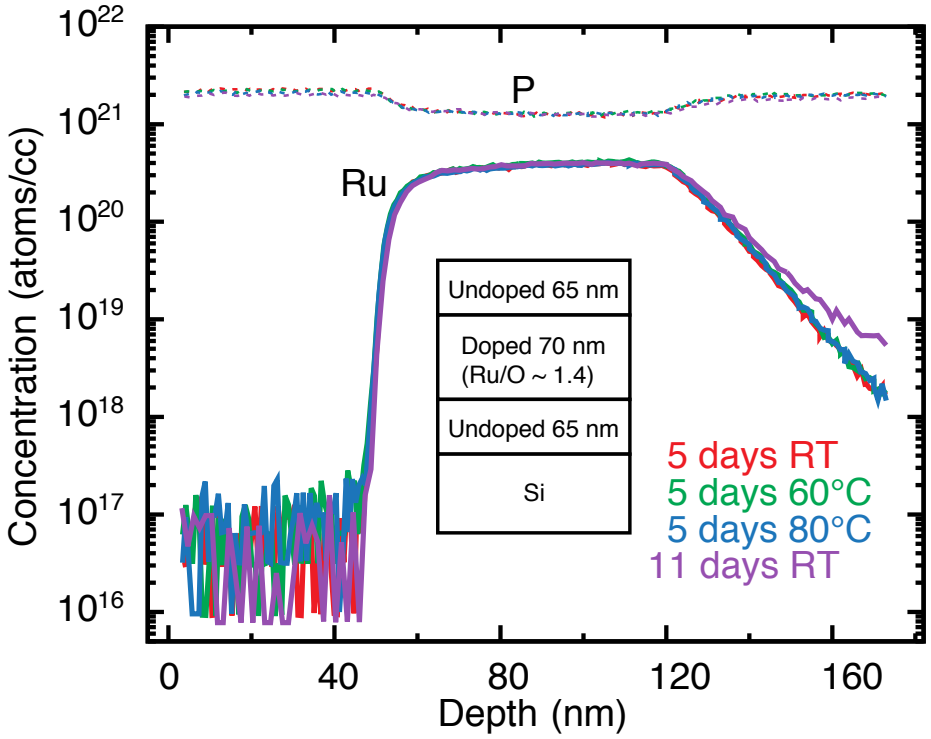


**Fig. S10:**
SIMS profiles of P (dashed lines) and Ru (solid lines) measured on a sample consisting of the following structure: undoped $POPy_2$ (65 nm)/doped $POPy_2$ (70 nm, Ru/O ~ 1.4)/undoped $POPy_2$ (65 nm)/Si (see inset). Red: measured five days following growth. Green/blue: same as red, but annealed at 60/80 °C for 30 min. Purple: same as red, measured 12 days after growth. The very sharp rise in Ru signal at a nominal depth of ~60 nm indicates an absence of $[RuCp^*Mes]_2$ diffusion into the top $POPy_2$ layer. The slower decay of the Ru signal on the other side of the doped layer (125 – 175 nm) is a snow-plowing artifact of SIMS and does not indicate dopant diffusion into the bottom $POPy_2$ layer. The slight decrease in P signal in the doped layer relates to the corresponding decrease in $POPy_2$ relative density.

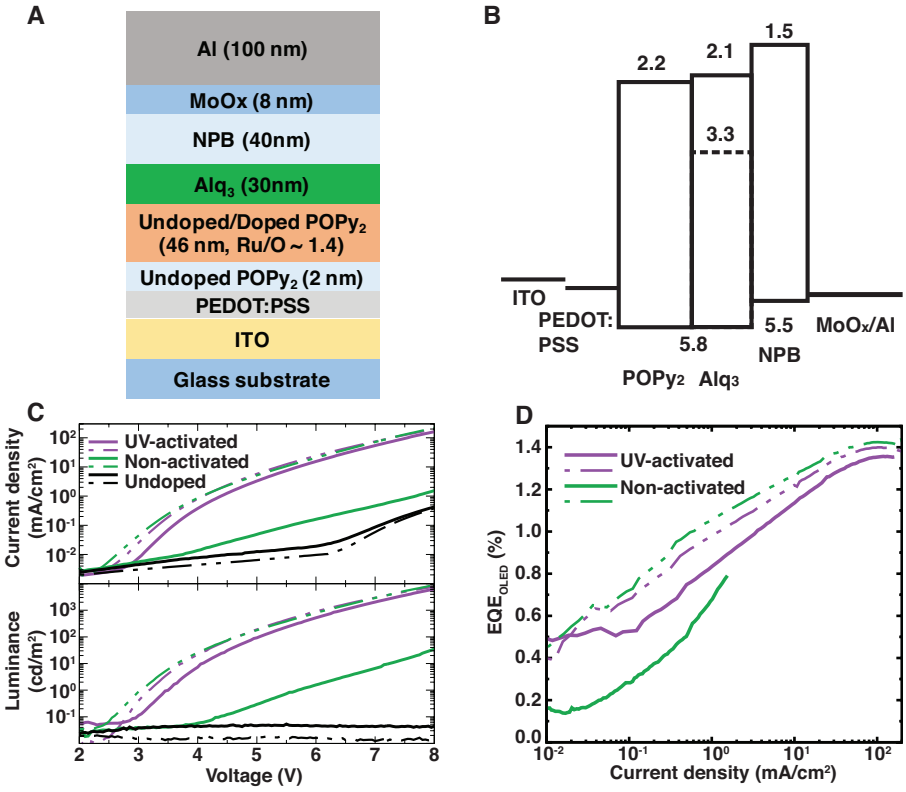


**Fig. S11:**

**(A)** and **(B)**: Structure and energy diagram of the OLED using $Alq_3$ as the emitter. The 2 nm undoped $POPy_2$ layer serves as a simple buffer that prevents co-evaporated dopants from reaching the PEDOT:PSS surface and changing its work function. The electronic structure and optical bandgap of $Alq_3$ are from ref. [36] and the electronic structure of NPB is from ref.[44]; **(C)** Current density (top) and luminance (bottom) vs. bias voltage of $Alq_3$ OLEDs built with undoped, non-activated doped, and UV-activated doped $POPy_2$ as ETL; **(D)** $EQE_{OLED}$ vs. current density of the same OLEDs. Full and dot-dashed curves correspond to 1st scan and 10th scan of the devices, respectively. The large difference between 1st and 10th scans for the doped but non-activated device reflects the self-activation discussed in the text.

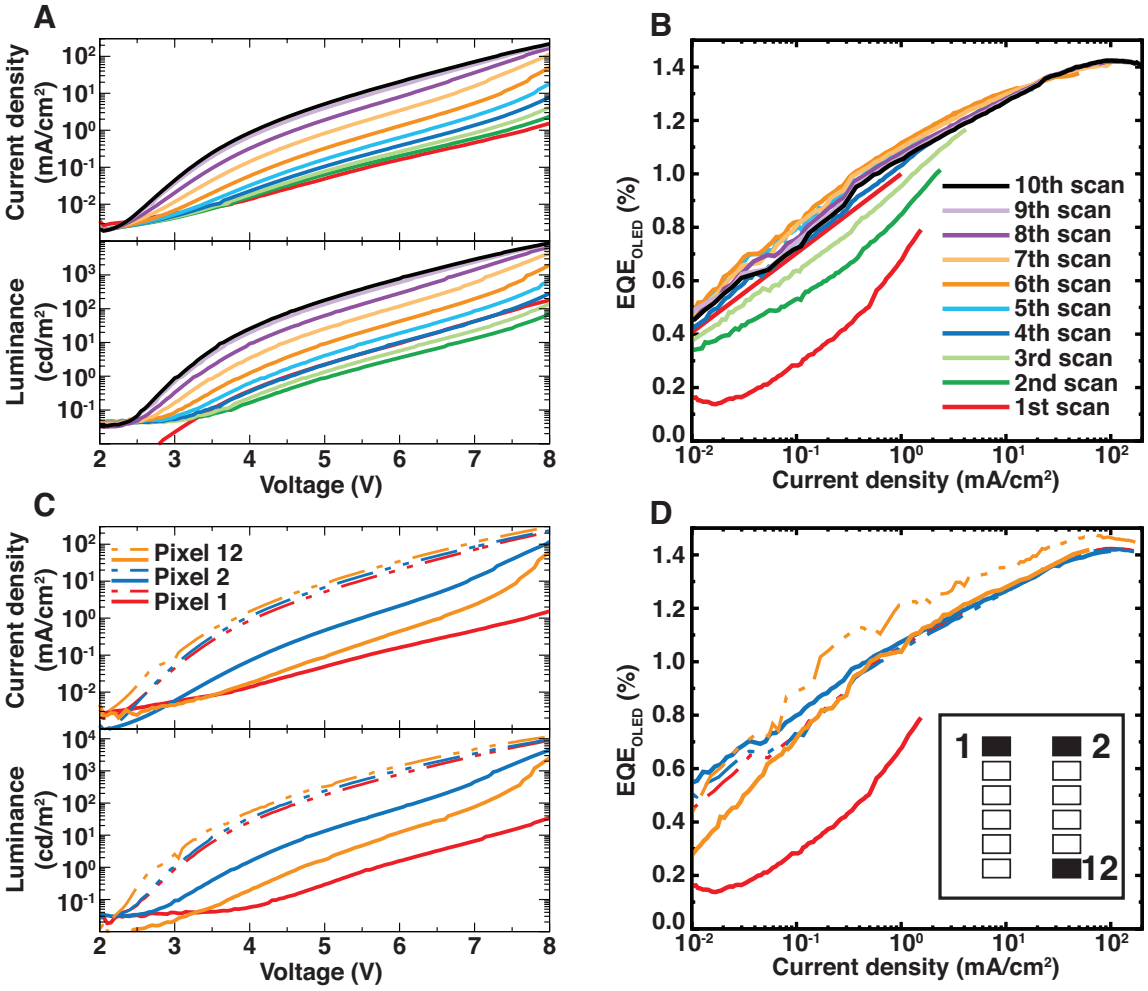


**Fig. S12:**

**(A)** Current density, luminance vs. voltage and **(B)** $EQE_{OLED}$ vs. current density of self-activation of doped $Alq_3$ OLEDs; **(C)** Current density, luminance vs. voltage and **(D)** $EQE_{OLED}$ vs. current density of three pixels, showing self-activation of doped $Alq_3$ OLEDs. The side length of the substrate is 3 cm and pixels are drawn to scale. Full and dot-line curves correspond to 1st scan and 10th scan of the device, respectively.

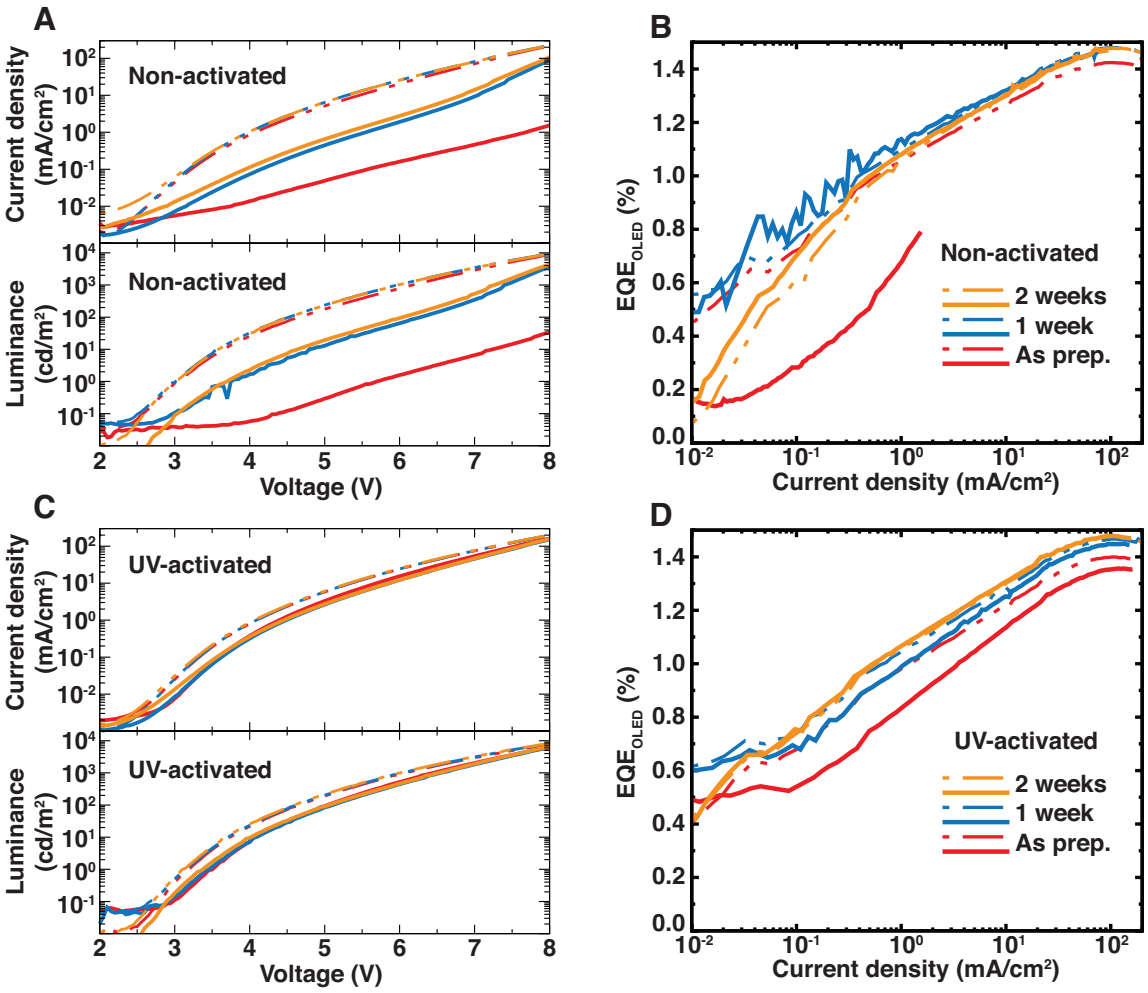


**Fig. S13:**
**(A)** Current density, luminance vs. voltage and **(B)** $EQE_{OLED}$ vs. current density of self-activated doped $Alq_3$ OLEDs in the course of two weeks. **(C)** Current density, luminance vs. voltage and **(D)** $EQE_{OLED}$ vs. current density of UV-activated doped $Alq_3$ OLEDs in the course of two weeks. Full and dot-line curves correspond to 1st scan and 10th scan of the device, respectively.

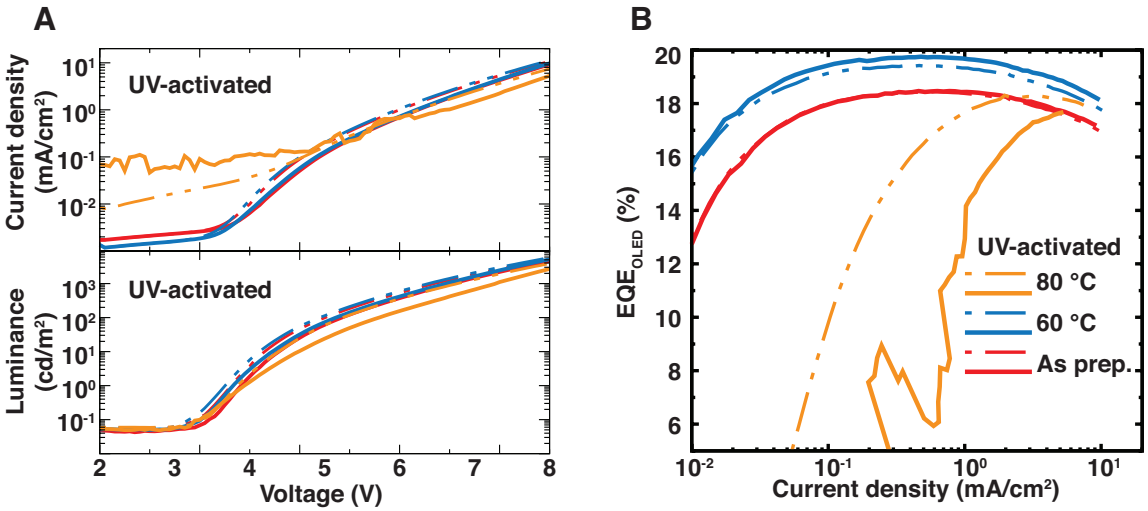


**Fig. S14:**
**(A)** Current density, luminance vs. voltage and **(B)** $EQE_{OLED}$ vs. current density of UV-activated TPBi:Ir(ppy)$_3$ OLEDs annealed at different temperatures for 30 min to test their thermal stabilities. Full and dot-line curves correspond to 1$^{st}$ scan and 10$^{th}$ scan of the device, respectively.

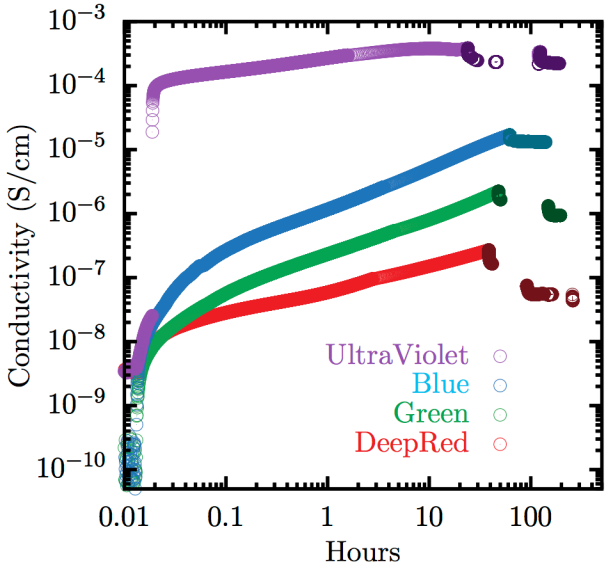


**Fig. S15:**
Fig. 2C presented on a log-log plot.

## Table S1.

Evolution of the WF of a doped $POPy_2$ (Ru/O = 0.86) film following IR and UV irradiation sequence. Since the resolution of Kelvin probe is around 0.1 eV, there is negligible change of WF under IR irradiation.

| | Before activation | 5 min IR | +20 min IR | +200 min IR | +2s UV |
|---|---|---|---|---|---|
| Work function (eV) | 3.4 | 3.4 | 3.3 | 3.3 | 2.6 |

## Table S2.

Evolution of the WF of $Alq_3$, c-HBC and ZADN films in terms of different activation sources.

| Materials | Activation | Red | Green | Blue | UV |
|---|---|---|---|---|---|
| $Alq_3$ [a] | Before activation | | 3.4 | | |
| | 2 s irradiation | 3.4 | 2.7 | 2.6 | 2.4 |
| | Few hours in dark [b] | | 2.5 (132) | | |
| c-HBC | Before activation | | 3.0 | | |
| | 5 min irradiation | -- | -- | -- | 2.6 |
| | Few hours in dark [b] | | 2.7 (40) | | |
| ZADN | Before activation | | 3.5 | | |
| | 5 min irradiation | 2.7 | 2.7 | 2.7 | 2.6 |
| | Few hours in dark [b] | | 2.8 (48) | | |

[a] The WF of undoped $Alq_3$ film is 4.4 eV.
[b] Number of hours is listed in parentheses.

## Table S3.

WF comparison between doped $POPy_2$ film with and without undoped $POPy_2$ as buffer layer.

| Ru/O ratio | | 0.66 | 0.79 [a] |
|---|---|---|---|
| Work function (eV) | Before activation | 3.0 | 3.2 |
| | 2 s UV | 2.6 | 2.5 |
| | 5 min UV | 2.5 | 2.4 |
| | Few hours in dark [b] | 2.6 (13) | 2.4 (27) |

[a] With 5 nm pristine $POPy_2$ beneath the doped film as buffer layer.
[b] Number of hours is listed in parentheses.

**Supplementary Information:**

## 1. Supplementary Methods

### 1.1. Materials and preparation

$p^+Si$ substrates with resistivity of 0.001 – 0.005 Ω·cm were used for electron spectroscopy and contact potential difference measurements. They were cleaned in sequential ultrasonic baths of acetone, isopropanol and methanol (each 10 min). After a 30 min UV-ozone treatment, a thin layer of PEDOT:PSS (Clevios™ P VP AI 4083, Heraeus GmbH & Co. KG) was spin-coated (5000 rpm for 40 s, 160 °C for 5 min) on top of the substrates, providing a smooth starting surface with a 5.1 eV WF. 10 nm of undoped or doped $POPy_2$ films (Luminescence Technology Corp., >99% purity) or $Alq_3$ films (Nichem) were then evaporated in UHV, and transferred under vacuum to the analysis chamber (base pressure of $10^{-10}$ Torr).

The quartz substrates used for conductivity measurements were purchased from GM Associates, Inc. They were cleaned with the same sequence as the Si substrates, then covered with interdigitated aluminum electrodes (100 nm thick, 150 μm inter-electrode gaps) and transferred to vacuum chamber under protection of nitrogen. Afterwards, 80 nm of undoped or doped $POPy_2$ or $Alq_3$ were deposited and conductivity measurements were done in the same vacuum chamber.

Non-activated dopant-containing films were obtained via co-evaporation of the host and the dopant, with the doping concentration initially determined by the relative evaporation fluxes of the two species controlled with a quartz crystal microbalance (QCM). The host flux was kept at ~ 0.3 Å/s for all samples in order to maintain a consistent film morphology. The dimer evaporation rate was controlled up to 0.03 Å/s to yield molar ratios between less than $10^{-3}$ and 0.1. The thickness of the film was taken in all cases to be that of the host because of the very small amount of dopants incorporated.

Samples for optical spectroscopy measurements were prepared similarly via (co-) evaporation by depositing various thickness of un-/doped $POPy_2$ on solvent-cleaned quartz glass substrates, respectively. Samples were then transferred from the vacuum system to a nitrogen filled glovebox (<0.1ppm $H_2O$, <0.1ppm $O_2$), where they were mounted into a small box containing two quartz glass windows for performing optical measurements under inert atmosphere. The sample with 10 nm $POPy_2$ is used to obtain photoluminescence spectrum of the host.

The photoluminescence spectrum of $[RuCp^*Mes]_2$ was obtain from a solution containing 1 mg/mL of dimer in chlorobenzene (PhCl). The solution was prepared in a nitrogen glovebox and transferred to air-tight quartz cuvettes for measurement.

For the $EQE_{PV}$ and OLED measurements, pre-patterned ITO substrates were sonicated in acetone and isopropanol for 15 min each. The substrates were then $O_2$-plasma treated for 5 min for further removal of surface contaminants and better wetting by PEDOT:PSS (only for OLEDs), which was spin coated at 2000 rpm for 30 s and baked at 100 °C for 10 min. The substrates were transferred to a vacuum thermal evaporator (EvoVac, Angstrom Engineering) with base pressure of around $8\times10^{-7}$ Torr for the deposition of:

1) $EQE_{PV}$ samples (Fig. S8): 2 nm of undoped $POPy_2$ as buffer layer, 46 nm of undoped or doped $POPy_2$, 10 nm BCP (bathocuproine, Nichem), and 100 nm aluminum (R.D. Mathis);

2) $Alq_3$ OLEDs (Fig. S11A): 2 nm of undoped $POPy_2$ as buffer layer, 46 nm of pristine or doped $POPy_2$, 30 nm $Alq_3$, 40 nm NPB (*N,N′*-di(1-naphthyl)-*N,N′*-diphenyl-(1,1′-biphenyl)-4,4′-diamine, Nichem), 8 nm $MoO_3$ (molybdenum(VI) oxide, Alfa Aesar), and 100 nm aluminum;

3) TPBI:$Ir(ppy)_3$ OLEDs (Fig. 5A): 2 nm of undoped $POPy_2$ as buffer layer, 46 nm doped $POPy_2$, 10 nm TPBi (2,2′,2"-(1,3,5-benzinetriyl)-tris(1-phenyl-1-*H*-benzimidazole), Nichem), 12 nm 8 wt% $Ir(ppy)_3$ (tris[2-phenylpyridinato-$C^2$,*N*]iridium(III), Nichem) doped TPBi, 15 nm TCTA (tris(4-carbazoyl-9-ylphenyl)amine, Nichem), 50 nm TAPC (4,4′-cyclohexylidenebis[*N*,*N*-bis(4-methylphenyl)benzenamine], Nichem), 5 nm $MoO_3$, and aluminum.

The doped $POPy_2$ for the $EQE_{PV}$ and OLEDs measurements gives Ru/O of 1.4.

$[RuCp^*Mes]_2$ was synthesized as previously described [31].

Measurements on dopant diffusion and concentration calibration were done at EAG laboratories via secondary ion mass spectrometry (SIMS) and Rutherford backscattering (RBS), respectively. Sample for SIMS analysis consisted of a three-layer stack with the following structure (Fig. S10): undoped $POPy_2$ (65 nm)/doped $POPy_2$ (70 nm, Ru/O ~ 1.4)/undoped $POPy_2$ (65 nm)/Si. Undoped layers and homogeneously doped layers were also prepared for SIMS calibration. Samples were measured either after 5 days or 12 days in the dark at RT; or following thermal treatment (60°C, 30 min., or 80°C, 30 min.). The SIMS calibration was also aided by a dopant concentration calibration performed via RBS on the Ru atom of the dopant.

### 1.2. General rules for experiments

To investigate the photo-activation of the dopants without interference from other energy sources, samples (both undoped and doped) were at all times protected from room light, light from the ion gauges, UV light, and X-ray and electron beams. Only a dim red flash-light was used to help with sample transfers and other manipulations. Ultra-violet photoemission spectroscopy (UPS), X-ray photoemission spectroscopy (XPS), and inverse photoemission spectroscopy (IPES) were only applied in special cases as indicated.

### 1.3. Optical absorption spectroscopy

Optical absorption spectroscopy was performed using a Lambda 950 UV/Vis/NIR spectrophotometer (Perkin Elmer Inc.). The spectra of thin films deposited on quartz glass substrates were recorded under controlled nitrogen atmosphere and light exposure. A baseline spectrum recorded from a clean quartz glass substrate was subtracted from the spectra before further analysis.

### 1.4. Photoluminescence (PL) spectroscopy

PL spectra were recorded using an Edingburgh FLS 980 spectrometer. An excitation wavelength of 340 nm was used for $POPy_2$ films, while 250 nm was used for $[RuCp^*Mes]_2$ solution, due to the negligible dimer absorption of photon energies less than 3.5 eV. The high excitation energy resulted in parasitic emission from the solvent (chlorobenzene), peaked around 300 nm, but no significant photoluminescence from the dimer was observed (the spectrum of pure chlorobenzene was subtracted as background).

### 1.5. Work function (WF) and contact potential difference (CPD) measurements

Neither UPS nor IPES was used to measure WFs, $E_F$ shifts in the gap or electronic structures of doped $POPy_2$ samples, as UV- or electron-irradiation from the He discharge lamp

(UPS) or the electron gun (IPES), respectively, would preempt the effect of controlled irradiation on the doped samples. CPD measurements in the dark and in UHV using a vacuum Kelvin probe were performed instead to follow the evolution of the sample WF and infer the shift of $E_F$. The WF of the probe was calibrated for each measurement using a vacuum-peeled highly ordered pyrolytic graphite sample (HOPG, Mosaic spread value of (0.8 ± 0.2)°, NanoAndMore Corp.), which provided a consistent WF of 4.55 ± 0.05 eV, as verified via UPS.

1.6. Conductivity and current-voltage (*I-V*) measurements

*I-V* measurements were also performed in UHV and in the dark to assess the conductivity of the $POPy_2$ thin films and the effectiveness of the dopants. The current through the layer was measured in the lateral direction. Following room-temperature deposition of the film, *I-V* measurements were recorded before and after activation in the same vacuum chamber, using a Keithley 2400 SourceMeter. Given the 150 μm inter-electrode gaps, applied fields did not rise above 6700 V/cm, which allowed a determination of the sample conductivity from the Ohmic region of the *I-V* characteristics. AFM measurements (using Veeco diInnova™) were done afterwards to confirm the thickness of the film.

1.7. Photo-activation

Irradiation was carried out using high power deep red, green, blue and UV LEDs (Thorlabs Inc.: M660L4, M530L3, M470L3 and M375L3, Fig. S3) operated at their typical currents. Samples in vacuum were activated in the vacuum chamber by illuminating through a normal Kodial glass window, which is transparent in the visible and UV region up to 300 nm (transmission of around 90%) with a distance about 12 cm between the LED sources and sample. The power density of LEDs at the sample was in the order of a few 100 $\mu W/cm^2$, but due to small changes in the exact setup (distance between the LED and the sample, sample tilt, etc.) could vary by a factor of 2 to 3.

For the control IR irradiation experiment (Fig. S5), we used a high power IR laser diode (Thorlabs Inc.: M9-940-0100, 940 nm (1.32 eV)) with the same setup as above.

For OLED devices, a 10 min UV irradiation sequence was used to activate doping in the glovebox after the deposition of the doped $POPy_2$ layer. The distance between the UV activation source and the sample was 8 cm.

1.8. Doping concentration determination and XPS

Throughout the experiments, the dopant incorporation in the molecular film was estimated using the ruthenium/oxygen (Ru/O) or ruthenium/nitrogen (Ru/N) ratio obtained via XPS (non-monochromatized Al-Kα – 1486.6 eV radiation). Ru is present only in the dimer, while O or N exists in most host materials. For C-only materials, such as c-HBC, we represented its dopant concentration using equivalent Ru/O in $POPy_2$ (Fig. S9). Unintentional surface accumulation of the dopants and difficulties in controlling the host-dopant co-evaporation complicated the precise determination of the dopant concentration, in particular in the low concentration regime. Nevertheless, the Ru/O ratio is found to scale monotonically with the molar ratios calculated from evaporation rates. Ru/O ratios between 0.05 and 1.40 approximately correspond to dopant-to-host molar ratios between $10^{-3}$ and 0.10. All XPS measurements were performed following all other measurements in order to avoid unintentional activation during data acquisition.

1.9. Determination of electronic structure of $POPy_2$ and UPS/IPES

UPS measurements were done with the He(I) photon line (21.22 eV) from a discharge lamp, with a -5 V bias applied to the sample to facilitate the observation of the photoemission cutoff. IPES, performed in the isochromat mode using a setup described elsewhere [45], was done in the same chamber. The resolutions of the UPS and IPES measurements were 0.15 eV and 0.45 eV, respectively.

### 1.10. Electrical and optical properties of OLEDs

The devices were measured in an $N_2$ glovebox using a calibrated silicon photodiode (FDS-100-CAL, Thorlabs), Keithley 2400 source-measure unit, picoammeter (4140B, Agilent), and a calibrated fiber optic spectrophotometer (UVN-SR, StellarNet Inc.).

### 1.11. $EQE_{PV}$ measurement

All EQE measurements were taken using a Newport TLS-300X tunable light source system. Measurements were taken under short-circuit conditions with a Stanford Research Systems SR830 lock-in amplifier and a SR570 current pre-amplifier to detect the photocurrent generated by the device from the incident chopped (110 Hz) monochromatic light source. A calibrated Si detector (Newport) was used as a reference cell. The luminance and the EQE of the undoped device are estimated using the spectrum and angular profile of the UV activated device.

### 1.12. Thermal stability test

UV-activated OLED samples were annealed on the hot plate in the glovebox after the deposition of doped $POPy_2$ for 30 min.

### 1.13. Cyclic voltammetry

Electrochemical data for $POPy_2$ were acquired using cyclic voltammetry in 0.1 M $nBu_4NPF_6$ in dry THF under nitrogen, using a CH Instruments 620D potentiostat, a glassy carbon working electrode, a platinum wire auxiliary electrode, and, as a pseudo-reference electrode, a silver wire anodized in 1 M aqueous potassium chloride solution. A scan rate of 50 mV/s was used and the potential was referenced to the ferrocenium/ferrocene couple by addition of ferrocene to the cell. Two successive reversible reductions were observed, the first of which, corresponding to the $POPy_2/POPy_2^{\bullet-}$ couple, was at a half-wave potential of –2.24 V vs. ferrocenium/ferrocene. Electrochemical data for the dopant system were taken from table S5 of ref [31].

## 2. Supplementary Discussions

### 2.1. "Contradiction" between unchanged conductivity and decreased WF on non-activated doped sample

Taking $POPy_2$ as an example, the WF and conductivity measurements performed on the non-activated doped samples (Fig. 2A) lead to an apparent contradiction, in that $E_F$ moves upwards in the gap by about 1.0 eV (to ~ 0.8 – 1.3 eV below the LUMO edge) without any significant change in conductivity. The lowering of the substrate WF by dopants was ruled out as an explanation for this behavior by introducing a 5 nm thick undoped $POPy_2$ interface buffer layer that only reduces the Fermi level shift by 0.2 eV (Table S3.). We therefore conclude that, without irradiation, the dimers can transfer electrons only to deep electron traps in the host gap, thus shifting $E_F$ and the WF without populating the shallower traps and LUMO states that form the charge transport manifold of the host material. $E_F$ prior to irradiation is several hundred meV

below these states, and the conductivity of $POPy_2$ remains unchanged. This interpretation is compatible with the effective reducing strength of $[RuCp^*Mes]_2$ originally deduced from CV and DFT, or from other doping studies (-2.04 V vs. $FeCp_2^+/FeCp_2$, or 2.8 eV to 3.0 eV).

## 2.2. Magnitude of conductivities via photo-activation with visible light

Close scrutiny of the data of Fig. 2C and similar data taken during the course of this work, including those on doped other host materials (Fig. S9), shows that the conductivities achieved with red, green and blue irradiation, under the conditions used here, does not saturate in the time allotted to the experiment, i.e. after 40 - 70 hours' irradiation. They appear to continue to increase, although exposure times necessary to reach the UV-activated conductivity level would be prohibitive for all. This is illustrated by presenting the data of Fig. 2C on a log-log plot (see Fig. S15).

In that regard, it is important to recall that the processes resulting from UV and (red, green, blue) activation are different. UV irradiation leads to Frenkel absorption in the host molecules, i.e. the overwhelming majority of the molecules of the doped film, and thus leads to a rapid electron transfer from all the dimers, followed by cleavage and doping (top of Fig. 3). On the other hand, red, green or blue irradiation leads to absorption exclusively in the already-weakly-absorbing CT states, and only at interfaces between the dimer and host molecules (bottom of Fig. 3, Fig. 4A). CT state absorption is therefore bound to be significantly smaller (by multiple orders of magnitude) than Frenkel absorption in the host, leading to a much slower rise in conductivity over time for a similar order of magnitude flux.

Additionally, activation by red light is likely to be much slower than by blue light. From an energetics point of view, the CT state absorption takes place in a joint manifold of Gaussian distributions of dimer HOMOs and host LUMOs in a predominantly amorphous system. Given the ~1 eV difference between the oxidation potential of the dimer and reduction potential of the host (Fig. 1), and a reorganization energy of ca. 1 eV associated with the dimer-to-host electron-transfer reaction (see the discussion in Supplementary Information Section 2.3), the deep red irradiation (620 nm, 2.0 eV) is at the limit of being able to generate CT state absorption with the majority of the dimers, thus drastically limiting the doping process and the film conductivity. To a lesser degree, the same can be argued for green and blue irradiation.

## 2.3. Reorganization energy

The maximum of donor-acceptor (D…A) charge-transfer-type absorption bands is observed at an energy $E_{max}$, where

$$E_{max} = E_{CT} + \lambda$$

where $E_{CT}$ is the energy difference between the neutral ground state (D…A) and charge-transferred excited state ($D^+…A^-$), both at their relaxed geometries. $E_{CT}$ can be estimated by the difference in IE(D) and EA(A), but may be somewhat lower in energy due to $D^+…A^-$ electrostatic interactions. Moreover, in a disordered film composed of anisotropic molecules a distribution of CT complexes with different geometries and $D^+…A^-$ interactions may be present. $\lambda$ is the relaxation (or reorganization energy, i.e. the difference in energy between the $D^+…A^-$ state at neutral and relaxed geometries. In the present case, if we estimate $E_{CT}$ from the electrochemical potentials given in Fig. 1B as $q(E(D^{2\bullet+}/D_2) - E(A/A^{\bullet-}))$, i.e. as 1.14 eV, then it is implied that $\lambda \sim 1$ eV. This value is larger than those obtained for a range of D:$C_{60}$ CT complexes from the lineshapes of the low energy tails (< ca. 0.6 eV and sometimes much lower)[46], although it is worth bearing in mind that the $C_{60}^{\bullet-}$ relaxation has a particularly small

influence on the lineshape. Quantum-chemical calculations suggest a contribution to λ of ca. 0.3 eV is expected for the dimer cation relaxation (see Table S5 of ref. [31]) and comparable values might be expected for $A/A^{\bullet-}$ by comparison with values for other electron-transport materials in the literature (e.g., for hexaarylsiloles [47]). On the other hand, the use of electrochemical values likely results in an underestimate of $E_{CT}$; a value based on solid-state IE and solid-state EA would be expected to be somewhat higher (since the ion states are less strongly stabilized by surrounding solid-state molecules than by polar solvent and electrolyte). Indeed, one can estimate the solid-state IE of the dimer as ca. 3.7 eV by comparison to that of rhodocene dimer [26], assuming the difference in dimer oxidation potential between the two dimers to be translated into a difference in IE. Taken in combination with the EA of $POPy_2$ (2.2 eV), one can estimate $E_{CT}$ = 1.5 eV, which suggests λ = 0.6 eV, more in line with precedent for solid-state CT complexes and with calculation.

2.4. Sensitivity of doped samples to oxygen

As expected from the low EA of the host material, doped samples (without any protective layer on top) were also found to be highly sensitive to oxygen. When kept in an inert atmosphere containing around 2 ppm oxygen, the conductivity decreased significantly over the course of several hours.